ARCADA

Bachelor's Thesis

Computational Fluid Dynamics and Aerodynamics-system identification of a real hexacopter for controlling the flight within urban environments.

Imteaz Morshed Joy

Bachelor Thesis

Mechanical & Sustainable Engineering

2024

Degree Thesis

Imteaz Morshed Joy

Computational Fluid Dynamics and Aerodynamics-system identification of a real hexacopter for controlling the flight within urban environments.

Arcada University of Applied Sciences: Mechanical & Sustainable Engineering, 2024

Identification number:

27613

Commissioned by:

Arcada University of Applied Science

Abstract:

This work presents a detailed computational fluid dynamics (CFD) simulation and aerodynamic investigation of a hexacopter both computationally and experimentally in an urban environment where the data is provided by the Doctoral Researcher, Michael Kurz (M.Sc), member of the aerospace faculty of the University of Applied Sciences Munich. This scientific work provides critical information regarding the flight behavior of a system identified hexacopter within the project "Einflussreduzierte Innerstädtische Luftransport Technologie" (ElLT). The aim of this project is to reduce the influence of urban conditions on air taxis and contribute to the current means of regulation to ensure safety to Urban Air Management (UAM). Therefore, the primary objective of this simulation is to enhance comprehension of the aerodynamic characteristics shown by the hexacopter, especially in low-level flight missions and urban landscape. Aerodynamic properties such as lift and drag coefficient $c_{x,}$ c_y *and* c_z by relating the drag forces to the dynamic pressure and reference areas in each direction, and moment characteristics $a_{x,}$ a_y *and* a_z of the hexacopter will be examined and determined. In order to simulate the airflow around the hexacopter, a numerical model is created utilizing the Navier-Stokes equations for fluid dynamics and conservation laws. The numerical model is done to attain the precise result by solving the mathematical calculations. The approach comprises several steps, such as geometry preparation, mesh construction, boundary condition establishment, and governing equation resolution. The utilization of Ansys Fluent is necessary for the generation of the numerical model. Various CFD techniques, such as Reynold-Averaged Navier Stokes (RANS) for turbulence flow field, have been employed in this work to examine the aerodynamics of the hexacopter.

.

Keywords: Computational Fluid Dynamics, RANS, Navier-Stokes, Hexacopter, Aerodynamics, Lift, Drag coefficient, Turbulence.

Table of Content

List of Figures

List of Tables

1 Introduction

Unmanned Aerial Vehicles (UAVs) have completely revolutionized the mapping and surveying industry by providing accurate topography data and detailed aerial photography (Ecko, 2023). Perhaps, military drones are mostly utilized for battle observation and tactical reconnaissance. Drones enable the military to access previously inaccessible regions and protect troops from unforeseen dangers (Telefónica, 2022). This thesis makes a valuable contribution to the field of UAV aerodynamics by providing a proven method for studying and forecasting hexacopter behaviour in urban settings. This method helps with the computational side of things, specifically with the design and optimization of more stable and efficient drones for different applications, by making use of ANSYS Fluent for computational fluid dynamics (CFD) analysis with turbulence models.

1.1 Background

Wind tunnel tests and flight trials have been the primary method to identify certain characteristics of aircraft for the last century and started to gain popularity with the Wright Brother in 1901, who researched aerodynamic parameters (Michael G & David, 2005). Especially UAVs are suited for physical tests and experiments within wind tunnels because of their constitution. Although these methodologies have produced valuable outcomes, they are not consistently cost-effective, time-consuming, and fail to encompass all conceivable configurations or operational scenarios. Moreover, there are logistical and safety concerns linked to carrying out experiments in actual environments, particularly in urban regions. As a result, the utilization of CFD for studying the aerodynamics of UAVs has gained significant popularity not the least, since one can simulate a wide variety of ideal environmental conditions for a specified object such as in this case urban constitutions influencing air taxis represented by a UAV hexacopter. CFD, which is numerical calculations of governing Navier-Stokes equations for the motion of viscous fluid, offers a cost-effective and efficient alternative to traditional testing methods by utilizing numerical techniques and algorithms to solve and analyze fluid flow problems (Sylvio R, 2017). Associated simulations of the airflow surrounding the hexacopter and analysis of the corresponding aerodynamic forces and moments can provide valuable insights into stability, control, and performance. Advancements in computational capabilities and simulation techniques have facilitated the application of CFD in the study of hexacopters and UAVs in general. Due to the utilization of

high-performance computing systems and sophisticated CFD software, researchers are now able to investigate intricate flow phenomena and conduct comprehensive evaluations of aerodynamics with unprecedented levels of accuracy and detail. Furthermore, the utilization of CFD empowers researchers to digitally optimize and evaluate UAV designs. This facilitates the controlled and replicable assessment of various configurations, control strategies, and operational conditions. This capability is particularly advantageous for studying UAVs in urban environments, where the aerodynamic efficiency can be significantly influenced by internal factors caused by the aircraft such as the downwash, outwash or ground effect and external factors implied by the environment such as turbulent airflow, proximity to structures, thermic variety, venturi effect or other air traffic members.
Still, a lot of research has to be done when it comes to system identification of UAV interaction with certain aerodynamic factors in contribution with CFD and identify the aircraft's aerodynamic behavior. Most of the time, the research has been carried out for the particular components of the aircraft such as different types and design of propellers, wings etc. For example (Henry, 2016), it has been identified the aircrafts aerodynamic behavior of the lifting surface on the UAV type flying wing. In another study, numerical analysis is conducted for the aerodynamics performance of two propeller designs at the static thrust condition to compare the thrust amount (Erdem & Junling, 2018).

In a similar vein, Smith used CFD to examine several winglet designs for tiny UAVs with the goal of improving performance (Smith & Brown, 2020). To minimize drag, Ahmed, Lee, and Wang used CFD to optimize the aerodynamic shapes of the UAV fuselage (Ahmed et al, 2019). Another study in the aerodynamics of multi-rotor and identified that various rotor blade tip designs significantly affect efficiency (Chen & Zhao, 2018). By optimizing the twist of propeller blades using computational analysis, it has been shown that UAV thrust, and efficiency could be improved (Gonzalez & Martinez, 2017). Lastly, for a better understanding of how different landing gear configurations affect UAV aerodynamics, scientists have performed CFD study which helped to improve design methods by lowering drag (Patel & Singh, 2021). In more recent time, CFD-based studies have focused on the aerodynamics of UAVs, namely quadcopters (Herath et al., 2021; Jin et al., 2021; Gao et al., 2021). It is noteworthy that most of these studies concentrated on UAVs in hypothetical environments, disregarding the challenges associated with urban locations, only.

Urban settings can challenge drones by navigating within unpredictable and intricate airflow patterns characterized by turbulent eddies, vortices, and flow separations. Issues pertaining to the safe and efficient operation of UAVs may develop when flow phenomena greatly impact their aerodynamic performance, stability, and control. By applying these principles to the simulation and analysis of airflow around UAVs, a greater understanding of them through the study of CFD can be acquired. Aerodynamic behavior is of the utmost importance in urban settings because buildings, trees, and other impediments impact airflow patterns (Ohashi, 2004). Within this thesis but also shown by the research, synthetic urban UAV airflow is the best represented by CFD models, including the impacts of turbulent eddies, vortices, and flow separations.

The unique aspect of the research conducted within this thesis is focused on the urban environment conditions, which plays a major role when it comes to the hurdles of urban air traffic management (UATM) legislation. The objective of this study is to investigate the behavior of aircraft in lower atmospheric conditions and urban areas, characterized by turbulent airflow caused by the presence of unstructured objects such as high-rise buildings and statues in different positions. Therefore, one can state, that this research differs greatly from the previous named studies, that primarily focus here is on the aerodynamics of UAVs within controlled and clinic environments only. Furthermore, this study partly uses real wind speed and wind direction data measured during flight done by the supervisor and the author within the frame of this thesis.

1.2 Objective

Drones and other UAV's play a crucial role in urban air mobility initiatives due to their versatile capabilities, enabling a diverse array of applications including airborne surveillance, package delivery, and infrastructure assessment.

A potential approach to address traffic congestion and to meet the growing need for efficient transportation systems for passengers but also delivery etc., in densely populated areas, is by mitigating disruptive parameters that have an impact on the flight performance as well as establishing traffic regulations and laws for urban air mobility (UAM). This solution enhances transportation accessibility while tackling the obstacles presented by urbanization. The integration of drones into urban airspace poses specific challenges due to the diverse and

dynamic nature of wind of urban environments. Drones operating in metropolitan areas encounter many atmospheric obstacles, including wind shear, turbulence, and localized flow disruptions caused by building structures and arrangement as well as different heat radiations by different materials (grass, cement, glass etc.). The effective and efficient utilization of UAVs in urban environments is contingent upon our comprehension of their aerodynamic properties. The desire for drone aerodynamics and performance can be enhanced by means of system identification, a process that entails the derivation of mathematical models from empirical data. The development of precise and anticipatory models for drone flight dynamics in urban environments can be facilitated through the utilization of system identification approaches, which involve the analysis of hexacopter reactions to environmental stimuli and disruptions. The Institute of Flight Dynamics Lab at Munich University of Applied Sciences is leading research on the flying characteristics and control of drones in urban environments. Cutting-edge experimental facilities and advanced modeling techniques are employed to accomplish this task. The laboratory's commitment to enhancing the effectiveness, reliability, and security of drone operations in urban settings is a crucial element of the urban mobility project governed by “EILT”.

This thesis seeks to contribute to the progress of urban air mobility by employing CFD and system identification approaches to analyze the aerodynamic performance of drones in urban contexts. This project represents a collaborative effort between a doctoral researcher and affiliated with the Institute of Flight Dynamics Lab. The objective of this research project is to enhance our comprehension of the complex interplay among urban airflow, air taxis, and simulation through state-of-the-art techniques. The techniques enable the secure and enduring incorporation of UAVs, also known as drones, into urban transportation networks. In addition, this thesis enhances the existing knowledge gap of urban related CFD studies with drones by considering low altitude flights scenarios combined with artificial and real measured (urban) wind data within the simulation.

1.3 Relevance to the degree programme

The degree in Mechanical and Sustainable Engineering is appropriate to research of this thesis on aerodynamics characteristics of UAVs operating in urban settings utilizing CFD. In this extent, the author contributes his knowledge of fluid dynamics, will get the chance to put the knowledge of fluid mechanics, which is a pivotal part of this degree program. In addition,

the thesis follows the concepts by investigating how UAVs might help with environmentally friendly transportation solutions, such as less traffic and less pollution by optimized path planning. Energy efficiency and resource optimization are crucial areas of Mechanical & Sustainable Engineering. Researching how UAVs interact with city infrastructure airflow also encourages the author to be resilient in the designs, which in turn leads to more durable solutions that can handle the stresses of city life. This, in turn, prepares the author for successful engineering careers where the author can make a difference in sustainable urban mobility and infrastructure development.

2 Literature

This chapter describes scientific basics within this thesis area's context. It shall provide an understanding for CFD modeling, offering a detailed explanation of its fundamental principles, governing equations, and approaches for modeling turbulence.

2.1 Computational Fluid Dynamics

Computational Fluid Dynamics is a fundamental method used to study and analyze fluid flow phenomena which initially started with 2D fluid flow in 1930. Based on Lewis Fry Richardson, the pioneering for CFD and numerical weather prediction, it has been implemented on around 1950 (Bhattacharyya et al., 2022). It provides a robust foundation for simulating and comprehending intricate aerodynamic behavior.

At the preliminary stage, CFD modeling involves solving the Navier-Stokes equations numerically, which describe how momentum, mass, and energy are conserved in fluid flow. The partial differential equations that govern the behavior of viscous fluid flows, which were for the first time described by Euler in 1752, the Navier and Stokes formed an equation by adopting Newton's definition and re-derived the formalism in 1845 by Stokes, which are then transformed into a set of algebraic equations that may be solved numerically (Sheng, 2020). These equations are discretized over a computational domain. The core principle of CFD is the partitioning of the computational domain into distinct parts or cells. Within these cells, the governing equations are solved in an iterative process to simulate the changes in flow variables across both spatial and temporal dimensions. The Navier-Stokes equations, when represented in differential form, play a fundamental role in CFD simulations by capturing the fundamental principles of momentum, mass, and energy conservation that govern the dynamics of fluid flow (Sylvio, 2017). In addition, the Navier-Stokes equations, when combined with constitutive relations such as the equation of state and viscous stress-strain connections, it effectively captures the fundamental principles of fluid motion and establish a mathematical structure for modeling various flow regimes by, encompassing both laminar and turbulent flows. Simplified versions of the Navier-Stokes equations, such as the RANS equations or the LES equations, are frequently utilized in practical CFD simulations. These simplified versions are chosen to strike a balance between computational cost and simulation fidelity, considering the flow characteristics and modeling objectives. In the case of turbulent

flow of air around certain shape characteristics, CFD proved to be a very suitable approach. In general, turbulence modeling techniques are employed to analyze the behavior of turbulent flow, which is a prevalent phenomenon in the field of fluid dynamics. Turbulence is known for its chaotic and unstable nature that has a significant impact on both aerodynamic performance and flow properties. The precise depiction of turbulence in CFD simulations is a significant computational obstacle, requiring the use of turbulence modeling tools to capture its impacts. The range of techniques employed in this study includes many approaches, which span from traditional Eddy Viscosity models like the Spalart-Allmaras model and k-ε model, to more advanced methods like LES and Detached Eddy Simulation (DES). Every turbulence model has unique assumptions and closure schemes that are designed to suit certain flow regimes and length scales. As a result, these models provide a balance between computational efficiency and accuracy. In brief, CFD modeling plays a crucial role as a diverse and essential tool for the simulation and analysis of fluid flow phenomena, encompassing the complex aerodynamics of hexacopters. Through the utilization of numerical methods, governing equations, and turbulence modeling techniques, CFD allows researchers to understand the intricate interaction of forces and moments that govern the motion of hexacopters. This, in turn, facilitates the optimization of design, assessment of performance, and control of flight for these aerial vehicles in various operating conditions.

2.2 Aerodynamics

Aerodynamics, the study of the motion of air and its interaction with solid objects, is fundamental to understanding the behavior of UAVs in urban environments. The field of aerodynamics, in relation to UAVs, encompasses the examination of the many forces exerted on the aircraft throughout its flight, such as lift and drag etc. The literature has shown multiple definitions of aerodynamics, highlighting its significance in the domains of aviation (Ideen, 2023). According to researcher (Anderson, 2015), aerodynamics is the scientific and engineering study of the movement of air around solid objects, with a specific focus on how the forces of lift and drag affect the flying of airplanes. According to another researcher (Katz & Plotkin, 2010), aerodynamics encompasses various domains, including aircraft design and wind energy amongst many others. Aerodynamic studies have been essential in UAV research to gain a deeper understanding of the complex interactions between their flight characteristics and the urban environment. Prior research has emphasized the importance of aerodynamic optimization in enhancing the performance and maneuverability of unmanned

aerial vehicles (UAVs). For instance, (Sreenath & Kumar, 2013) a study conducted on the dynamics, control, and planning involved in cooperative manipulation of payloads suspended by cables from multiple quadrotor UAVs which are needed to control hexacopter dynamics. Furthermore, advancements in CFD have facilitated the ability of researchers to simulate and investigate the airflow of UAVs with unprecedented levels of accuracy and intricacy, thereby revolutionizing the field of aerodynamic analysis. The utilization of CFD models in investigating the influence of turbulent airflow on UAV aerodynamics provides valuable insights into the complex interplay between UAVs and their urban surroundings. Critical insights into stability difficulties were used CFD simulations to study the impact of urban canyon turbulence on the flight dynamics of UAVs (Turgut & Karakoc, 2014). The aerodynamic performance of UAVs in urban areas is studied using CFD, focused on how building-induced turbulence affects flying efficiency (Shi et al. 2017). To better understand how wind gusts affect tiny UAVs, identified disturbances which are used to improve control algorithms and make UAVs more resilient in urban airspaces (Kim & Gharib, 2019).
This literature analysis is to establish a foundation for future research in the domain of urban aerodynamics by presenting a comprehensive survey of the scholarly literature pertaining to the subject matter and its relevance to investigations involving UAVs.

2.2.1 Hexacopter Aerodynamics

Hexacopters, as multirotor aerial vehicles with the composition of six rotors, also known as hexacopters, rely on aerodynamic principles to generate lift and control their motion. Understanding the aerodynamic forces and moments acting on a hexacopter is a crucial aspect for optimizing its performance and stability (Mane, 2023).

The lift and drag coefficients, denoted as c_l and c_d respectively, are fundamental parameters that characterize the aerodynamic performance of a hexacopter. Lift is the force perpendicular to the relative airflow that opposes the weight of the hexacopter, enabling it to stay airborne. Drag, on the other hand, is the aerodynamic resistance encountered by the hexacopter as it moves through the air (Lift & Drag, 2017).

Determining the lift and drag coefficients involves experimental testing, computational simulations, or a combination of both approaches. Wind tunnel experiments provide empirical data on the aerodynamic behavior of hexacopter configurations under controlled

conditions. CFD simulations offer a computational framework for predicting these coefficients by solving the governing flow equations around the hexacopter geometry.
In addition to lift and drag, hexacopters experience moments around their principal axes – pitch, roll, and yaw. These moments are essential for controlling the orientation and stability of the hexacopter during flight.

- Pitch moment: A moment around the lateral axis, influencing the nose-up or nose-down rotation of the hexacopter.
- Roll moment: A moment around the longitudinal axis, causing the hexacopter to tilt sideways.
- Yaw moment: A moment around the vertical axis, leading to the rotation of the hexacopter in the horizontal plane.

The distribution of these moments is influenced by various factors, including rotor configuration, airfoil design, and flight dynamics (Lift & Drag, 2017). Understanding the aerodynamic characteristics governing these moments is crucial for designing efficient control algorithms and achieving stable flight performance.

Hexacopters, equipped with six rotors arranged in a symmetric configuration, offer advantages in terms of redundancy, stability, and payload capacity compared to quadcopters or other configurations. The positioning of rotors, along with their individual thrust characteristics, affects the aerodynamic forces and moments acting on the hexacopter. Optimizing the rotor configuration involves balancing lift distribution, minimizing drag, and maximizing control authority. Advances in rotor design, such as variable pitch propellers and ducted fans, further enhance the aerodynamic efficiency and maneuverability of hexacopters.

2.3 Laws of Conservation

In subsection 2.3 titled "Laws of Conservation," will go over the basic rules that control how physical quantities act in fluid dynamics. Among these responsibilities is the clarification of the essential concepts for comprehending fluid flow phenomena: the conservation of mass, momentum, and energy. The continuity equation, which states that mass is conserved, proves that mass is constant in a fluid flow. The transmission of momentum inside a fluid medium is demonstrated by the conservation of momentum, which is described by the Navier-Stokes equations. The energy equation, which is a common representation of the principle of

conservation of energy, also explains the transformation and conservation of energy in a fluid system. Many technical and scientific fields rely on these rules as a theoretical basis for studying and forecasting fluid dynamics.

2.3.1 Integral & Differential Form

The conservation equations can be derived in integral and in differential form of aspects. The integral form is derived by the utilization of a control volume. The fluxes are balanced and brought into equilibrium using surface and volume integrals, which are numerically employed in Finite-Volume Methods (FVM). In the context of finite difference methods (FDM), the derivation of the differential form is achieved by the employment of an infinite volume element and is numerically implemented (see in Fig. 1 Usage of Integral and Differential form (Ferziger & Peric, 2002)) and are described by the following mass conservation of integral form:

$$\frac{Dm}{Dt} = \frac{D}{Dt}\iiint \rho \, dV = \iiint \frac{\partial \rho}{\partial t} \, dV + \iint \rho(\vec{\mu} \cdot \vec{n}) \, dS \tag{1}$$

The momentum conservation of integral form can then be described by:

$$\iiint \rho\vec{\mu} dV = \iiint \frac{\partial(\rho\vec{\mu})}{\partial t} dV + \iint \rho\vec{\mu}(\vec{\mu} \cdot \vec{n}) dS = \iint \vec{t} \, dS \, dV + \iiint \rho\vec{f} \tag{2}$$

Fig. 1 Usage of Integral and Differential form (Ferziger & Peric, 2002)

With regard to time, the rate of change of mass within a control volume is represented by Dm/Dt in Equation (1), which explains the conservation of mass. Both the internal mass change rate and the net mass flux over the volume's boundary are included in the equation. By considering both the time-dependent variation of momentum and the flow of momentum over the volume border, Equation (2), relevant to momentum conservation, calculates the rate of change of momentum within the control volume. In this context, μ stands for the field of

vectors representing velocities, ρ for densities, n for the outward unit normal vector on the surface, and $\vec{f}$ for external body forces that operate on the fluid.

The differential form, which is called FVM, is utilized throughout the entire calculation in order to model and simulate the motion of fluid. The differential equation can be derived by applying a mass balance to a separate infinite volume element and is described by mass conservation of differential form below followed by Fig. 2:

$$\frac{\partial \rho}{\partial t} + \nabla \cdot (\rho \vec{\mu}) = \frac{\partial \rho}{\partial t} + \frac{\partial}{\partial x}(\rho u) + \frac{\partial}{\partial x}(\rho v) + \frac{\partial}{\partial x}(\rho w) = 0 \quad (3)$$

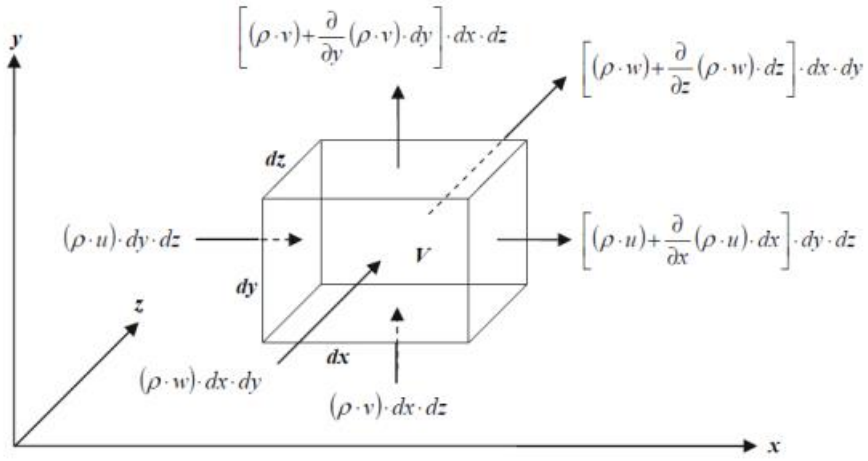

Fig. 2 Mass conservation derivation in a 3D volumetric dimension (Ferziger & Peric, 2002)

Therefore, momentum conservation of differential form can then be described by the following with respect to Fig. 3:

$$\rho \frac{D\vec{u}}{Dt} = \rho \vec{f} + \nabla \cdot \boldsymbol{T} \quad (4)$$

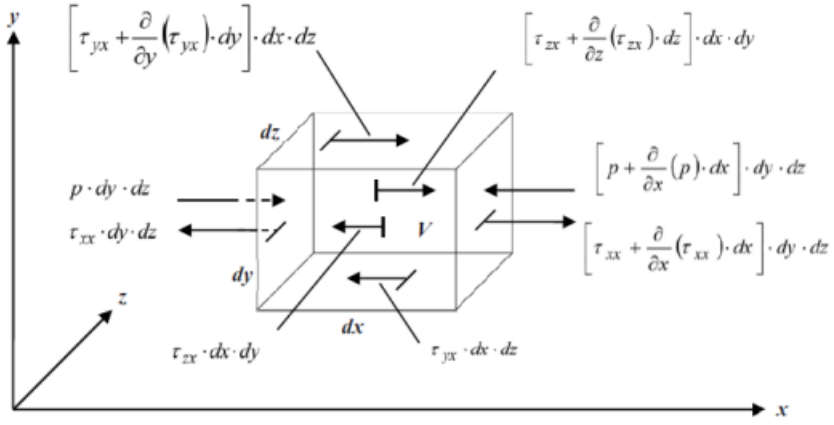

Fig. 3 Momentum conservation derivation in a 3D volumetric dimension (Ferziger & Peric, 2002)

2.4 Numerical Method

This chapter describes how to solve fluid flow problem or object in fluid dynamics.

2.4.1 Numerical Mesh

The generation of the numerical mesh holds significant importance in the field of CFD as it serves to partition the problem domain into distinct elements, such as volumes for three-dimensional (3D) problems, surfaces for two-dimensional (2D) problems, and edges for one-dimensional (1D) problems (Ferziger & Peric, 2002). The process of differential equations governing fluid flow is solved using a method known as domain discretization, which involves the creation of computational points referred to as nodes (Versteeg & Malalasekera, 2007). The feasibility of mesh design is facilitated by the ability to build nodes of variable form and quantity (Anderson, 1995). While the term "volume" may lack precision when referring to 2D and 1D areas, it is widely accepted that the area between these nodes is commonly referred to as a control volume.

The computational domain utilised in the CFD simulation encompasses the numerical mesh, which comprises the summation of all control volumes (Hirsch, 2007). This domain can consist of either a single fluid volume or many domains that contain different fluids (Ferziger & Peric, 2002). It is also feasible to establish solid domains devoid of fluid, such as walls of a specific thickness. The energy equation is the only one that needs to be solved, together with any potential domains of fluids, in order to enable heat transfer, diffusion, and electrochemical reactions (Patankar, 1980).

The gradients of variables such as velocity within the domain exhibit variations, which can be attributed to events such as boundary layers and shocks (Anderson, 1995). In order to accurately capture the flow behaviour, it is imperative to consider these alterations in the mesh design (Hirsch, 2007). However, this presents several supplementary demands, including the need to strike a balance between computational resources (namely, memory usage and processing time) and the imperative for accuracy and resolution (Versteeg & Malalasekera, 2007). The identification of this optimal point is of utmost importance in the development of effective and reliable CFD models that accurately represent the fluid dynamics within a given region.

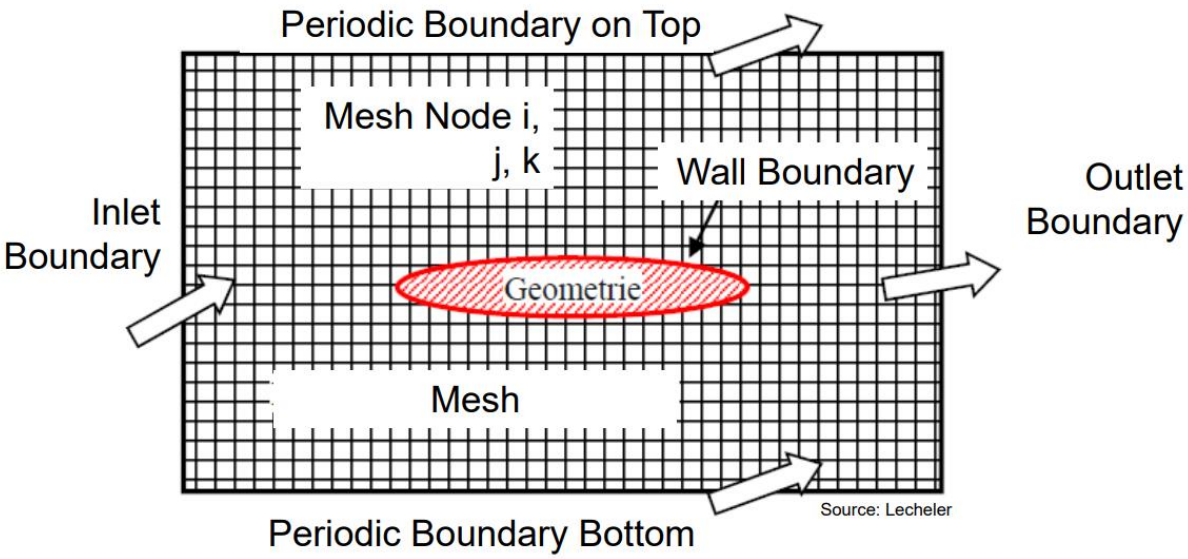

Fig. 4 Computational meshes of external flow around a body (Lecheler, 2022)

Two distinct approaches for generating numerical meshes, structured block meshes and unstructured meshes, are applied. Each method has a unique grid layout (see in Fig. 5 & Fig. 6) and possesses its own distinct collection of components. Structured block meshes exhibit distinct connections among their nodes and possess a well-organized, grid-like configuration (Hirsch, 2007). The meshes can be further classified into further grid types, namely O-grids, C-grids, and H-grids. O-grids, composed of many layers of cells surrounding an object, provide enhanced resolution for complex geometries. C-grid cells that adhere to the boundaries of the geometry enable smoother transitions between areas. The cells in close proximity to the object exhibit seamless transitions as they distance themselves from the cell, resulting in H-grids that combine elements of both O- and C-grids. A boundary-adapted mesh is a structured mesh that adjusts the size and form of its cells near its boundaries to accurately

represent flow characteristics. Unstructured meshes, as opposed to conventional grid connections, facilitate the random interconnection of nodes (Thompson, Soni, & Weatherill, 2016). While these meshes may require more computational resources, they offer greater flexibility in dealing with complex geometries and flow characteristics. Hexahedra, tetrahedra, and prisms are frequently employed as fundamental components in the construction of unstructured meshes. Hexahedral elements, which are Polyhedra with six faces, excel in terms of numerical accuracy and efficiency. While tetrahedral components, which consist of four vertices and four faces, may require finer meshes to achieve the same level of accuracy, they are highly versatile and perform effectively with irregular geometries. Prism elements, resembling wedges or pyramids, are commonly used in solving for the boundary layer in an unstructured mesh due to their ability to effectively capture flow gradients near surfaces.

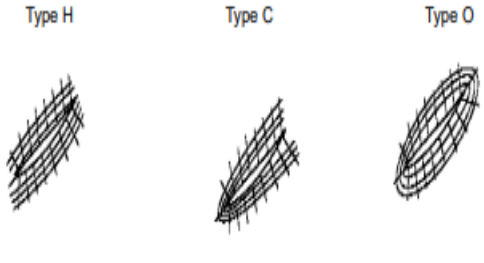

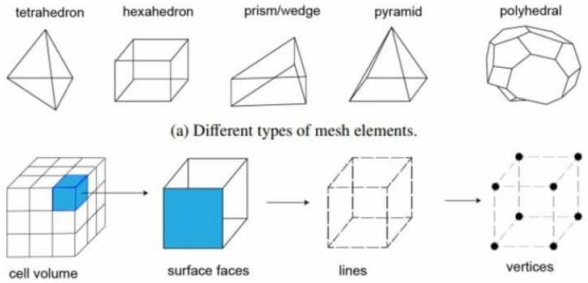

Fig. 5 Types of meshes (Mbehroozjl, 2022) *Fig. 6 Mesh elements (Mbehroozjl, 2022)*

Several techniques are used to construct computational fluid flow approximations, while coordinate transformations are employed to produce C-grids (if author needs to make specific grid), along with additional methods and elements. The "paving" process, commonly seen in CFX's meshing tools which were not used in this hexacopter modeling, serves as a viable substitute for O-grids in the generation of volume meshes (Yongcai, 2016). Commercial meshing solutions, such as ICEM CFD, provide a diverse array of grid generation capabilities (*Introduction to Ansys ICEM CFD*, n.d.). The aforementioned capabilities encompass structured grids, namely H-, O-, and C-grids. Hexahedra serve as fundamental units in structured and block-type meshes, however they can be subjected to certain twisting techniques.

The utilization of tetrahedra as fundamental components for unstructured meshes is widespread due to their ability to provide straightforward volume filling, as exemplified in the game Tetris, while also offering effective contour correction (Boutchko et al., 2013). Prisms play a key role in both structured and unstructured meshes. Prisms (see in Fig 1.5) are

used in unstructured meshes to create inflation layers for boundary layer modeling, ensuring accurate representation near the wall. Prisms can be utilized to create hybrid meshes that integrate the most advantageous aspects of both structured and unstructured approaches (Sun et al., 2017).

2.4.3 Finite Difference Method

For an extended period, FDMs have been recognized for their ability to solve one-dimensional systems and problems involving partial differential equations (PDEs) in a direct, precise, and consistent manner (Santana et al., 2022). The differential terms of this equation are converted into linear algebraic equations known as finite-difference equations through discretizing the continuous domain using FDM. The equations (3 & 4) exemplify how this approach facilitates the depiction of heat transfer phenomena in both solid and liquid states by solely addressing dependent variables at specific sites (Santana et al., 2022).

Although FDMs have demonstrated effectiveness in solving fluid flow problems for conventional geometries, their performance may be limited when applied to domains characterized by non-standard shapes (Santana et al., 2022). To achieve more accurate outcomes, one can readily increase the order of the distinct elements by employing a FDM, which commonly separates the mathematical and physical model on a dimensional basis. Conversely, FDMs may encounter difficulties in incorporating more distinct components in areas with intricate forms and managing interruptions caused by geometry (Pulliam et al., 1999). Despite the limitations imposed by regular or block-like flow domains, FDMs remain a valuable computational simulation technique (Santana et al., 2022). A descriptive representation would be from generalized transport equation (5) of differential form:

$$\frac{\partial(\rho\varphi)}{\partial t} + \frac{\partial}{\partial xi}(\rho\varphi ui) = \frac{\partial}{\partial xi}[\Gamma\frac{\partial\varphi}{\partial xi}] + S\varphi \qquad (5)$$

The mathematical derivation can be achieved via Taylor series expansion and Polynomial ansatz depicted in Fig. 7 (*Solving Dynamic Equations in Dye Transport, 2014, Ferziger & Peric, 2002*).

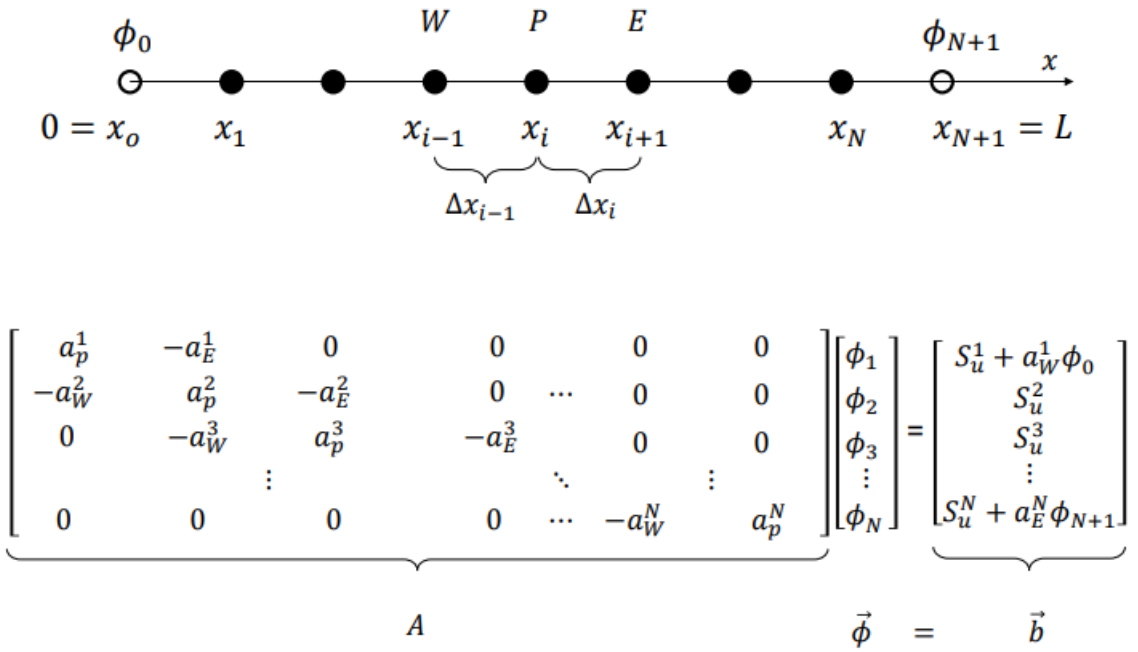

Fig. 7 The matrix derivation of FDM (Ferziger & Peric, 2002)

Fig. 7 represents the mathematical execution for the discretization of the PDEs up to assembly of the system of equations which includes insertion, sorting and evaluation.

2.4.4 Finite Volume Method

The Finite Volume Method (FVM), developed by McDonald and MacCormack in the early 1970s, served as a fundamental basis for CFD simulations and significantly transformed numerical methods for solving fluid flow problems (McDonald & MacCormack, 1971). Irrespective of the mesh topology, the FVM used a more adaptable strategy compared to its previous iterations by partitioning the domain into finite volumes. Also due to its adaptability, it effectively addressed intricate geometries and flow conditions seen in practical engineering scenarios (*The Finite Volume Method in Computational Fluid Dynamics*, n.d.). The theoretical foundation for the numerical solution in FVM is derived from the integral form of the conservation laws (see chapter 2.3), which are fundamental to the field. The computational domain of FVM ensures the preservation of mass, momentum, and energy (Versteeg & Malalasekera, 2017). This is achieved by partitioning the domain into control volumes and estimating fluxes across the boundaries of these volumes. This approach maintains the physical significance of the numerical solution while preserving the conservatism of continuum mechanical concerns. Recent developments in CFD have elevated the application of FVM to a higher level in various disciplines. Research has focused on

enhancing the accuracy and efficiency of FVM solvers through the development of novel numerical schemes and algorithms (Iaccarino & Vermeire, 2003). Investigations have been conducted to extend the spectrum of applications for FVM and to include multiphase flows, turbulent flows, and complex geometries (Peric et al., 2017; Moukalled et al., 2016).

A mathematical representation would be from generalized transport equation of integral form is described by the following equation:

$$\iiint \frac{\partial(\rho\varphi)}{\partial t} dV + \iint \rho\varphi u_i n_i \, dA = \iint \Gamma \frac{\partial \varphi}{\partial x_i} n_i \, dA + \iiint S\varphi \, dV \quad (8)$$

The Fig. 8 provides visualization adheres to a cell-centered layout, which is used in most CFD applications for FVM. The proposed configuration involves a grid node that functions as the central point for each control volume (CV). The east, west, north, and south sides of the CV are denoted by small letters, (such as *e*, w,n,s) in a two-dimensional representation. In addition, capital letters are employed to indicate the neighboring control volumes in each direction. For instance, in the context of two-dimensional representation, the control volumes to the east, west, north, and south are denoted as *E, W,* □, *S* respectively. The utilization of a cell-centered structure is prevalent in CFD simulations in FVM method due to its facilitation of the process of discretizing the governing equations and determining fluxes at the interfaces of the control volume.

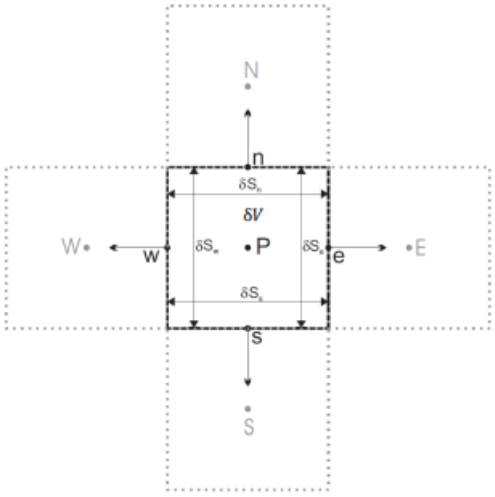

Fig. 8 FVM control volume demonstration (Ferziger & Peric, 2002)

For volume integrals, the discretization of the finite volume method is typically accomplished through the use of the center-point rule, which is of the second order:

$$\iiint (Su + Sp\varphi)\, dV \approx (Su + Sp\varphi p)\delta V \tag{9}$$

The complete system described for the FVM can be seen in Fig. 9.

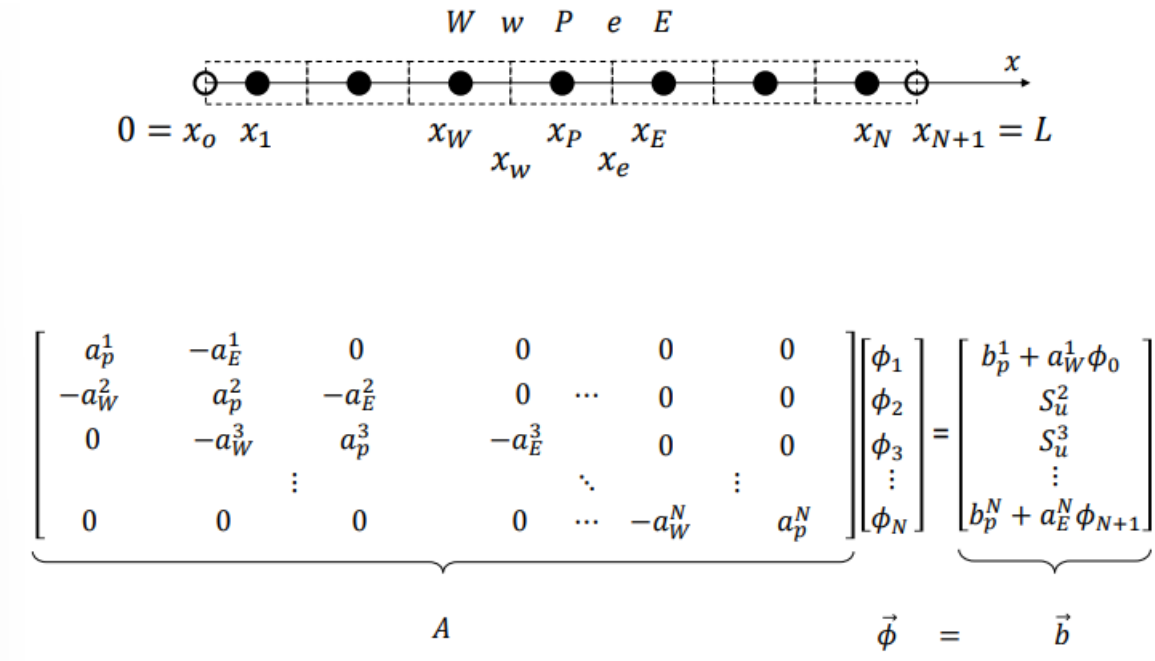

Fig. 9 The matrix derivations of FVM (Ferziger & Peric, 2002)

The FVM yields an equation system (see in Fig 1.9) for equidistant mesh designs, akin to the outcomes obtained by the FDM. An important differentiation is in the positioning of the cell centers. While FDM often employs node-centered designs, FVM utilizes a cell-centered structure. Equations are employed to define the conservation of mass, momentum, and energy within the control volumes, while the fundamental concepts and methods of discretization remain consistent (Liu & Hu, 2018). In non-equidistant mesh topologies, where grid spacings and cell sizes are not consistent, the differences between FVM and FDM become more noticeable. FDM uses the same approximation techniques to compute fluxes across control volume interfaces, while FVM utilizes distinct formulas, leading to alternate methods of discretization. This variation can impact the efficiency and accuracy of the numerical solution, particularly in regions characterized by spatial gradients or non-standard geometries. Despite these variations, the FVM ensures the preservation of mass conservation inside the computational domain and maintains its conservativity while dealing with continuum mechanics problems. The preservation of the physical integrity of the depicted system is ensured by enforcing mass conservation equations in each control volume, resulting in conservativity (Li & Wang, 1999). Hence, the FVM remains a robust numerical technique for

simulating fluid flow and transport processes, offering physically significant solutions for numerous scientific and engineering inquiries.

2.4.5 Time Discretization

Time discretization is essential when addressing CFD problems in FVM or FDM method related to steady-state flows. In order to progress the solution over time, it is imperative to introduce a discretization of the time factor within the governing equations. Differentiation quotients, such as those employed in the FDM, the FVM, and the Finite Element Method (FEM), can be utilized to achieve temporal discretization in a manner analogous to their facilitation of spatial discretization (Gottlieb & Ketcheson, 2016).

The initial point for temporal discretization is the generalized transport equation, which is expressed in integral form for a spatial FVM discretization. The equations 12 illustrate the temporal variation of the quantity:

$$\iiint \frac{\partial(\rho\varphi)}{\partial t}\, dV = - \iint \rho\varphi u_i n_i\, dA + \iint \Gamma \frac{\partial\varphi}{\partial x_i} n_i\, dA + \iiint S\varphi\, dV \tag{12}$$

Considering the characteristics of the source, convective, and diffusive terms within the control volume. There are several approximation strategies available for generating the discrete form of the time derivative, including forward Euler, backward Euler, Crank-Nicolson methods and Runge-Kutta Methods (Ascher et al., 1997). These strategies are contingent on the desired stability and precision of the numerical solution. The utilization of time discretization in the field of CFD enables the representation of non-stationary fluid flow through the iterative evolution of the solution over time, achieved by approximating the temporal components of the governing equations.

The linear system of equations that has been produced as a result and needs to be solved appears to be the same for all discretization methods (see Fig. 10).

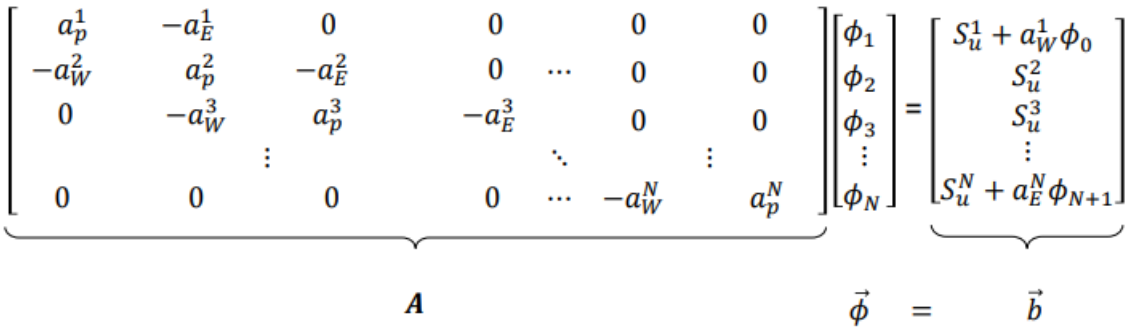

Fig. 10 Matrix form of discretization methods

2.4.6 Pressure-Velocity coupling

The concept of pressure-velocity coupling holds significant importance in the simulation regarding the hexacopter, which delves into the intricacies of drone aerodynamics. Pressure-velocity coupling is a crucial element in maintaining the coherence of pressure and velocity fields across the fluid domain. This is vital to uphold the fundamental principle of mass conservation and ensure the convergence and stability of numerical solutions. In drone aerodynamics, the efficacy of pressure-velocity coupling algorithms is significant due to intricate phenomena such as turbulent airflow interactions and vortices. The utilization of these methods is crucial for the precise representation of the intricate flow physics associated with flight, hence enabling the realistic simulation of the aerodynamic characteristics shown by drones.

The accuracy and reliability of CFD models have been significantly enhanced by contemporary techniques for establishing a connection between pressure and velocity. The development and enhancement of algorithms such as Semi-Implicit Method for Pressure-Linked Equations (SIMPLE) and Pressure Implicit with Splitting of Operators (PISO) have made noteworthy progress (Serra & Semião, 2021). The algorithms offer sophisticated techniques for iteratively adjusting the pressure and velocity fields, resulting in numerical solutions that are both more precise and computationally efficient (Ferziger & Perić, 2002).

To map the effects of correlation between the structural dynamics of drones and the aerodynamic forces will be achieved by employing advanced coupling approaches to CFD models of drone aerodynamics, with a particular focus on urban environments.

The SIMPLE algorithm is used to derive the discretized and the momentum discretized equation arranged by:

$$u_{i,j} = \frac{\sum anb\,.\,unb + bij}{aij} + \frac{Ai,j}{ai,j}(P_{I-1,J} - P_{I,J}) \tag{14}$$

and:

$$v_{I,j} = \frac{\sum anb\,.\,vnb + bI,j}{aI,j} + \frac{Ai,j}{ai,j}(P_{I,J-1} - P_{I,J}) \tag{16}$$

For a better understanding, the process of the SIMPLE algorithm is shown in Fig. 11.

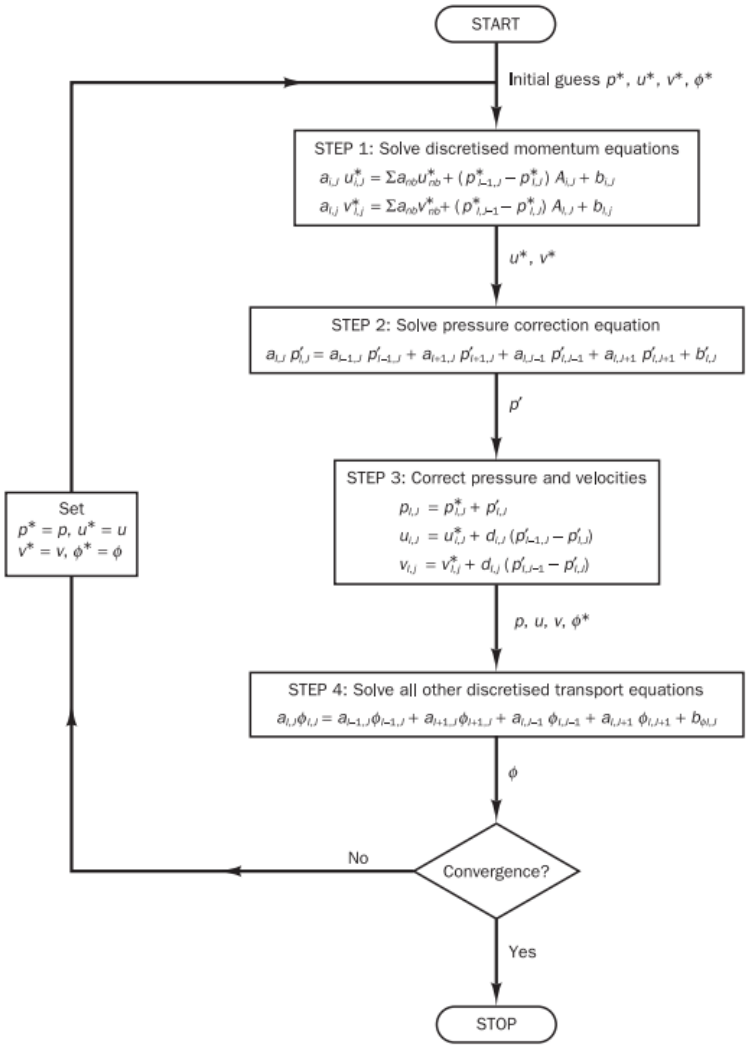

Fig. 11 Simple algorithm of pressure-velocity coupling (Ferziger & Perić, 2002).

2.5 Turbulence Modelling

The Navier-Stokes system of partial differential equations governs turbulent flows, such as laminar flows. The incorporation of convection elements in turbulent flows results in the transformation of the Navier-Stokes equations into a non-linear dynamic system. Under specific conditions, this system exhibits deterministic chaotic qualities to distinguish turbulent flows from fully random events. Significantly, the deterministic chaos theory imparts a deterministic characteristic to turbulent flows by suggesting that simulations conducted in an identical manner yield consistent results.

Turbulence arises from a disparity between the forces of friction, which induce damping, and the impacts of convective transport, which induce disturbance inside the flow. These two physical aspects interact intricately with one another. When the significance of friction and convective transport diminishes, the flow undergoes instability, leading to the emergence of small-scale oscillations known as Tollmien-Schlichting waves (Ferziger & Perić, 2002). The occurrence of this instability leads to a sudden and significant alteration in the flow, resulting in turbulence characterized by irregular motion patterns and unpredictable fluctuations.

The application of a tailored stability analysis to the specific flow configuration and conditions is of utmost importance in assessing whether a flow regime exhibits turbulent characteristics. Assessing the proportional contributions of various forces and transport processes within the flow is essential for determining the onset of instability and turbulent transition. Once the flow enters an unstable phase, characterized by a greater emphasis on convective transport rather than damping effects, it rapidly transitions into a turbulent state.

This state is described by an individual critical value of the Reynolds number:

$$R_e = \frac{uL}{v} = \frac{\rho uL}{\mu} = \frac{imertial\ forces}{friction\ forces} \tag{17}$$

Since turbulent flows are highly transient, Osborne Reynolds demonstrated decomposition of a transient quantity and its average value which can be derived by:

$$\bar{\varphi}(x_i,t) = \lim_{n\to\infty} \frac{1}{N} \sum_{n=1}^{N} \varphi_n\,(x_i,t) \tag{18}$$

By turbulent diffusion, turbulence brings fluid of differing momentum content into contact. The kinetic energy of the flow is diminished during the process of mixing due to the influence of viscosity, which serves to decrease velocity gradients. The dissipated energy undergoes an irreversible conversion into the internal energy of the fluid.

2.5.1 Reynolds-Averaged Navier-Stokes (RANS) model

Flow instability is averaged using Reynolds-averaged techniques to turbulence, such as the RANS equations. This gives an accurate representation of the flow. Because the Navier-Stokes equations are non-linear, this averaging approach is necessary to accurately describe turbulent flows due to non-linearity of the equations generated terms. Due to the intrinsic complexity of turbulence, it is highly unlikely that a single Reynolds-averaged model will be able to fully capture all processes that occur in turbulent flow. As a result, turbulence models are more correctly described as engineering approximations than scientific concepts set in stone. The scalar quantity of the mean equation can be expressed as:

$$\frac{\partial(\rho\bar{\varphi})}{\partial t} + \frac{\partial}{\partial x_j}(\rho\bar{u}_j\bar{\varphi} + \rho\overline{u_j''\varphi''}) = \frac{\partial}{\partial x_j}(\Gamma\frac{\partial\bar{\varphi}}{\partial x_j}) \quad (19)$$

All of the variables in equation (19) are responsible for a flow that is statistically constant can be described by the sum of their time-averaged value and the volatility that they exhibit around that value. In order to ensure that the time averaging is performed over a suitably large period, T, the interval must be sufficiently large in relation to the normal time scale of the oscillations. Ensemble averaging, on the other hand, is utilized in situations when flows are unstable. This technique includes conducting an average calculation across many flow realizations to smooth out bumps along the way. Applying one of these averaging methods to the Navier-Stokes equations allows for the possibility of "re-averaged" (or "re-averaged") the equations. As a result, the RANS equations are generated.

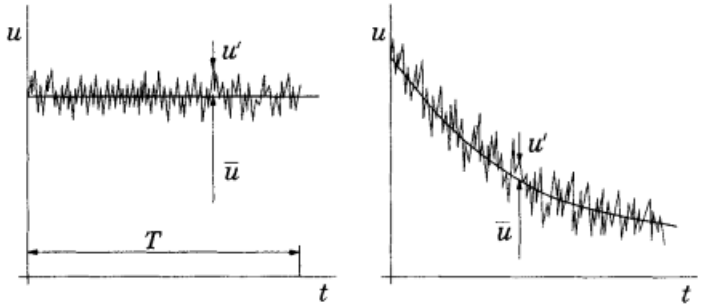

Fig. 12 Time averaging for steady and unsteady flow (Ferziger & Perić, 2002)

The act of averaging results in the production of additional components in the conservation equations, such as turbulent scalar fluxes and Reynolds stresses can be seen Fig. 12. These components cannot be uniquely described by the mean values alone since they involve the averaging process. These terms are the result of the nonlinearity of the equations and the correlations between the many flow variables present in turbulent flows. This results in the conservation equations becoming open, which means that they contain more variables compared to formulation in (19). It is required to use approximations in order to solve (19). Some examples of these approximations include prescribing the Reynolds stress tensor and turbulent scalar fluxes depending on the mean flow variables.

The Reynolds stress tensor and other higher-order correlations each have their own set of equations that can be derived; however, these equations introduce new unknown correlations that require further assumptions to be made in the model. After everything is said and done, it is not possible to obtain a closed set of accurate equations for turbulent flows. The approximations that are utilized to address this issue are referred to by a couple of different names: parametrizations in the geosciences and turbulence models in engineering. Due to the fact that they assist in predicting the behavior of turbulent flows, these models are extremely useful tools for a wide variety of scientific and technical fields that deal with turbulent flows.

3 Method

In chapter 3, the research methodology and procedural framework are explained in detail. The author outlines the strategies used to accomplish the research goals and highlights the results to the questions. It usually includes a comprehensive account of the software and hardware used in computational simulations or experimental setup.

3.1 Wind-gust testing for the urban airflow identification

In order to acquire data on the wind gusts that drones experience during flight an especially in urban airflow settings, specifically their identification and quantification, a physical drone equipped with wind sensing capabilities is utilized. This drone is called “Optokopter” and is the first of its kind. It is capable of measuring the wind during movement neglecting the airspeed with a measurement frequency of about 20 Hz in real time. A certain period of the Munich universities airport facility in Oberpfaffenhofen/Germany (see in Fig. 13) is utilized for the purpose of carrying out field experiments in order to collect data. This location is selected because of its exposure to a variety of wind patterns and the presence of buildings, especially hangars that have the potential to produce turbulent airflow resembling urban air conditions and shapes.

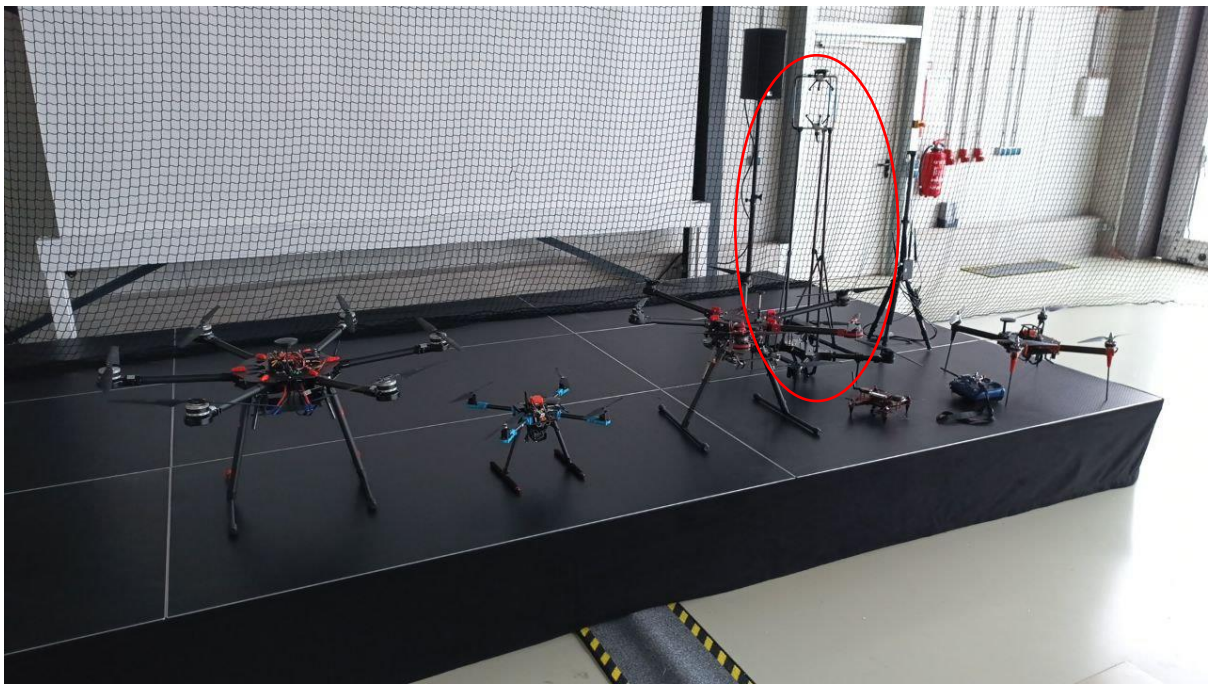

Fig. 13 Exemplary depiction of Munich university research drones as well as the Optokopter (marked in red) stored at their airport hangar in Oberpfaffenhofen, Germany

It is necessary to carefully record differences in wind speed and gusts during the trial flights. This is accomplished by flying the drone along predetermined flight courses at 3 m predetermined heights. The flight paths of the aircraft are meticulously planned to ensure that they travel through regions characterized by wind barriers and turbulence caused by buildings. Since this is part of the project “EILT”, no further explanation of the flight missions is provided, but it shall be mentioned, that dedicated data is provided specifically for this thesis. The data has been gathered with great care. It is specifically the hangar's architecture that made it possible to identify individual wind gusts during adverse weather. It is worth to be noted, that the placement of the ultrasonic anemometer on the “Optokopter” at precise location along flight routes is crucial, due to downwash or interaction with buildings and is one approach for acquiring data. This sensor is used to detect wind factors such as speed and direction.

With the assistance of the physical drone and the strategic experimental setup, wind gusts in urban airflow are effectively recognized and quantified. This can be considered a significant achievement in the grand scheme of things. The obtained data not only helps to shed light on the intricate dynamics between wind and man-made structures, but it also eased up the process to create tactics that could alleviate the negative impact of turbulent airflow to the handling and steadiness of unmanned aerial vehicles.

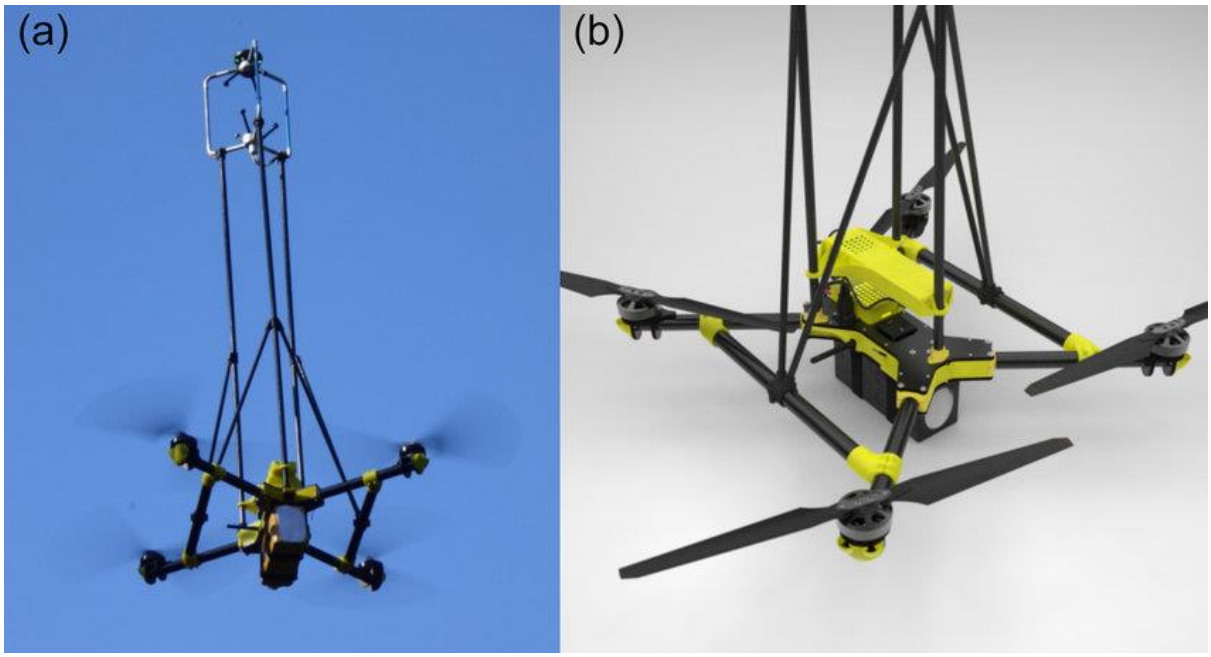

Fig. 14 Optokopter drone during flight (a) and at ground (b)

3.2 Computational Processing

This chapter demonstrates the complete computational work in ANSYS software as well as Python for data visualization.

3.2.1 Geometry setup and repairing

The geometry mending stage is an essential part of the research process. It plays a significant role in assuring the precision and dependability of the CFD study that is carried out with ANSYS Fluent. To begin with, it is of the utmost importance to underline that the actual measurement of wind in an urban area has been carried out. In general the subsequent analysis is mostly computational. The Computer-Aided Design (CAD) model of a hexacopter (seen in Fig. 15), which is the primary focus of the investigation, is brought into ANSYS Fluent for the purpose of conducting an analysis for system identification purposes. It is important to take note of the fact that the CFD analysis is carried out using ANSYS Fluent.

Fig. 15 Imported CAD model in ANSYS Geometry

The workflow in ANSYS Fluent begins with the selection of the Fluid Flow module, which is then combined with Fluent Meshing. This combination makes it possible to investigate the flow behavior surrounding the hexacopter. Importing the CAD model of the hexacopter into the geometry module of ANSYS Fluent is the first operation that needs to be completed. After that, the geometry is subjected to a variety of alterations and edits by making use of the "DesignModeler" tool contained in the geometry work-package in ANSYS. These activities are done according to the research objectives. To be more specific, the focus is placed on aligning the plane and axis in X, Y, Z in co-ordinate direction (local & global) of the drone, in addition to the components that map the drone, such as the main body and the six propellers.

Additionally, holistic attempts are made to address any inconsistencies or unwanted sketches found within the geometry. This entailed the removal and repair of unidentified sharp geometries and unnecessary components housed in the drone body. These components include antennas, wire connections, and internal components. After the geometry is meticulously fixed and adjusted, the subsequent phase is the demarcation of the domain that is either fluid or solid. As a result of the fluid dynamics character of the issue, the majority of the domain is dedicated to the examination of fluid flow. Following the completion of the domain segmentation, an enclosure that is created to resemble a wind tunnel is built in order to recreate the flow environment around the hexacopter. This enclosure has well delineated boundaries for the intake and outflow, which allows the airflow to be controlled across the computing area. A favorable environment is built for the purpose of conducting complete CFD simulations in order to examine the aerodynamic performance of the hexacopter under a variety of wind conditions. This is accomplished by creating the wall boundaries below and designing the domain in accordance with them.

Boundary parameters;

- Initial Position
    a) X = 10m
    b) Y = 20m
    c) Z = 5m
- Initial Orientation
    a) Roll 0 degrees
    b) Pitch 0 degrees

c) Yaw 90 degrees

- Average velocity considered
  a) Velocity – 10m/s
  b) Angle of attack – 15 degrees
- Environment profile
  a) Temperature – 25 degree celsius
  b) Pressure – 1013 hpa
  c) Humidity – 65%

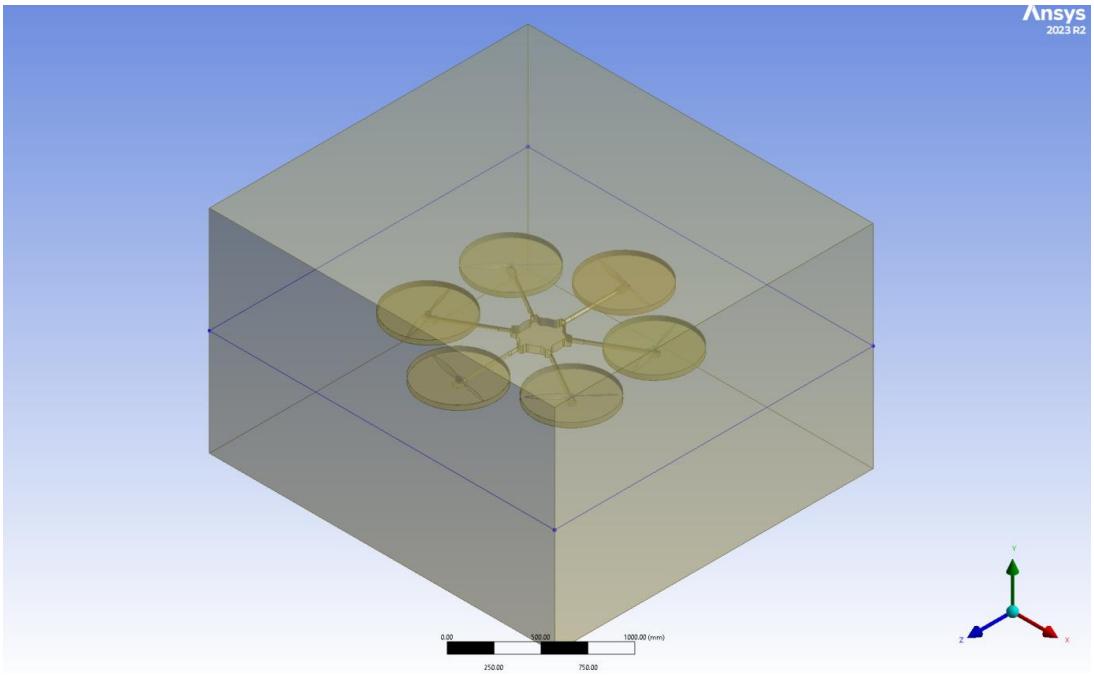

Fig. 16 After repairing enclosure and domain was created around the hexacopter geometry

3.2.2 Mesh Sizing

CFD simulations like ANSYS Fluent rely heavily on mesh sizing to guarantee accuracy and fidelity. To numerically solve the governing equations of fluid flow, mesh scaling is an essential part of numerical modeling since it discretizes the computational domain into finite elements. Mesh sizing methodology is crucial for capturing the detailed flow phenomena surrounding the aerial vehicle in the present study. Finding the sweet spot between computing efficiency and solution, adjusting the resolution in an iterative process is the procedure for mesh sizing, a multi-stage process that involves methodically exploring and optimizing mesh parameters. In order to tailor the mesh to the analysis's unique needs, the author has access to

a wealth of mesh control. The major goal for mesh sizing is to reduce the computational domain to a manageable number of elements while capturing all the intricate flow characteristics and phenomena that come with the hexacopter's aerodynamic behavior.

Step one in starting the mesh sizing process in the fluent environment is to define the geometry of the hexacopter and its surrounding enclosure. To do this, one needs to import the hexacopter's CAD model and set up the appropriate coordinate systems to properly orient the geometry. The next step is to examine the geometry closely for any intricate features or imperfections that could require extra care during meshing. In order to generate and enhance meshes later on, these first processes are necessary.

The process of mesh sizing relies on assigning named selections to specific geometry components. One way to modify and manage the mesh precisely is with named selections, which is to describe specific regions of interest inside the geometry. Propellers1, Propellers2, Propellers3, Propellers4, Propellers5, Propellers6, the main body, the inlet, the outlet, and other relevant elements are given named selections (see Fig. 17) within the context of the hexacopter study. This fine-grained control makes sure that the mesh is fine-tuned at locations where geometric complexity or flow gradients are complex and keeps a coarser mesh when computing resources are not so important.

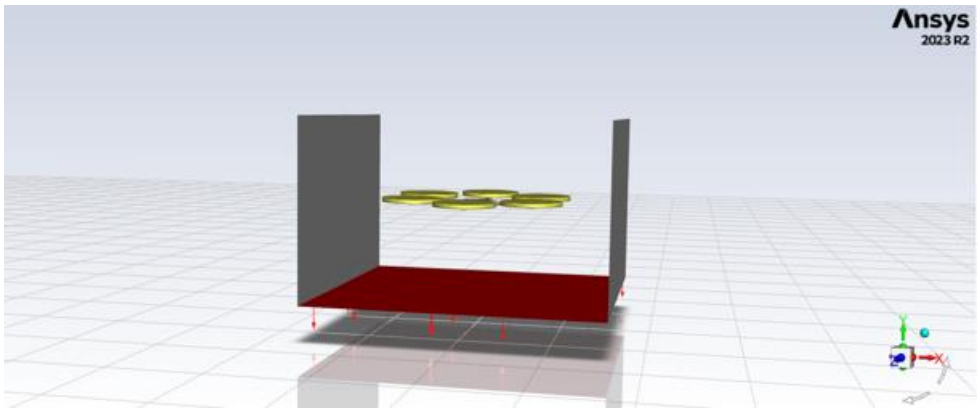

Fig. 17 Name selected and meshed propellers.

As the author proceeds to the meshing phase, plenty of choices for controlling and generating meshes are available. In this case, the mesh is adjusted to meet the needs of the analysis by specifying the number of elements, element size, and other meshing parameters. Finding an optimal trade-off between mesh resolution and computational cost is carefully considered for the current study, which calls for investigating several mesh phases from coarse to fine. A try

and error method for identifying optimal resolutions within the simulations lead to a careful selection of 804996 nodes and 4376969 elements.

When starting to generate a mesh, it is common practice to use a coarse mesh to approximate the flow field surrounding the hexacopter. In order to pinpoint which areas, need a finer mesh resolution, a coarse mesh as a foundation for further optimization and refining is used. In order to prepare for potential flow separation or vortical structures, the mesh is iteratively refined in key places, such as those close to the hexacopter's surfaces.

When determining the optimal size of a mesh, it is crucial to consider the flow physics and the behavior of the boundary layer when choosing the boundary conditions and mesh settings. As part of the hexacopter study, the computational domain's inlet, and outlet borders (encounter, left and right) are set to simulate the flow conditions encountered by the aerial vehicle while in flight. The choice of turbulence models and solver parameters is also carefully considered to provide accurate and reliable simulations.

Using both qualitative and quantitative criteria, including cell volume ratio, aspect ratio, and mesh skewness, to assess the created meshes quality and sufficiency as the mesh scaling process advances (see in Fig. 18).

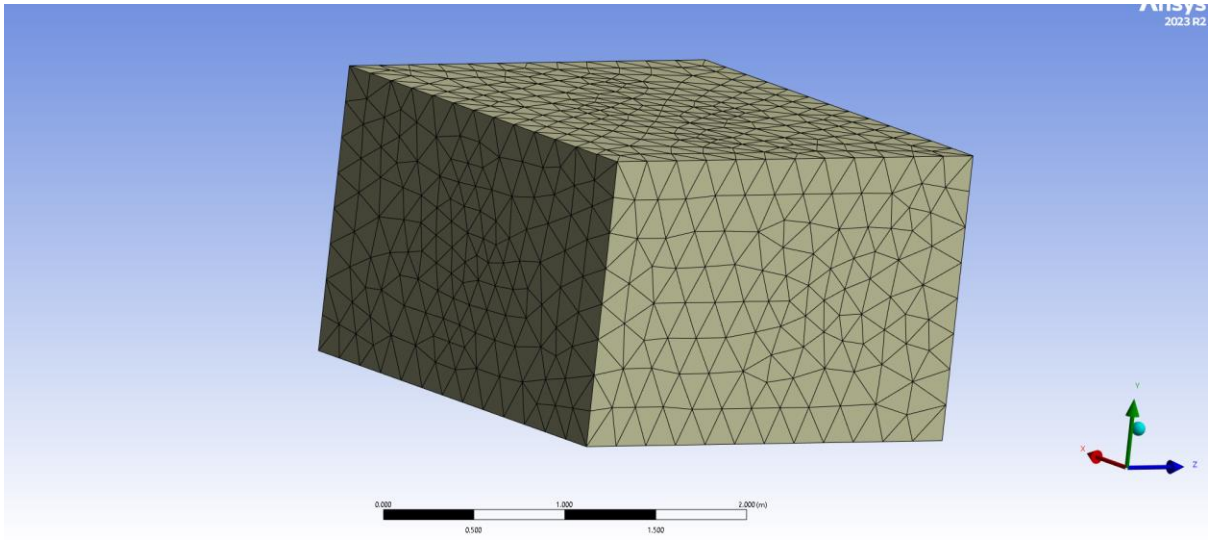

Fig. 18 Generated Mesh over my domain

To ensure that the final mesh accurately represents the flow field while keeping computational cost to a minimum, the balance between mesh resolution with computational cost throughout the mesh sizing process has to be ensured. To achieve accurate and reliable CFD simulations, it is necessary to improve and optimize the mesh iteratively. This allows a

thorough investigation of the hexacopter's aerodynamic performance under different flow conditions.

Mesh sizing is an essential part of CFD numerical modeling since it guarantees the computational domain to be discretized and the numerical solution of fluid flow equations to be performed. Optimizing computing efficiency while accurately representing flow events is possible through a systematic approach to mesh generation and refinement, to adjust the mesh to the unique requirements of the investigation. In this instance, the meshing strategy for the computational domain that encompassed the hexacopter is an unstructured prism mesh that is deployed inside the enclosure. The decision is made because of the exceptional characteristics of the flow field; more specifically, there are no geometric features or objects in close proximity to the hexacopter, which means that the flow environment is relatively continuous and unhindered. Utilizing an unstructured prism mesh allows for the discretization of the computational region surrounding the hexacopter in a manner that is both cost-effective and efficient. This mesh is beneficial for capturing flow behavior in huge regions largely devoid of obstructions. The geometry of the hexacopter and the flow domain that surrounds it are painstakingly tracked by the high-quality elements that are generated by the unstructured prism mesh contained within the enclosure. Both the precise simulation of boundary layer behavior and the high-fidelity recording of near-wall flow dynamics are possible because of the prism layers, which are aligned with the flow direction. Both of these processes are carried out simultaneously. This particular meshing method performs exceptionally well in situations when there are no geometric impediments or disturbances, and the flow field displays very little fluctuation or turbulence.

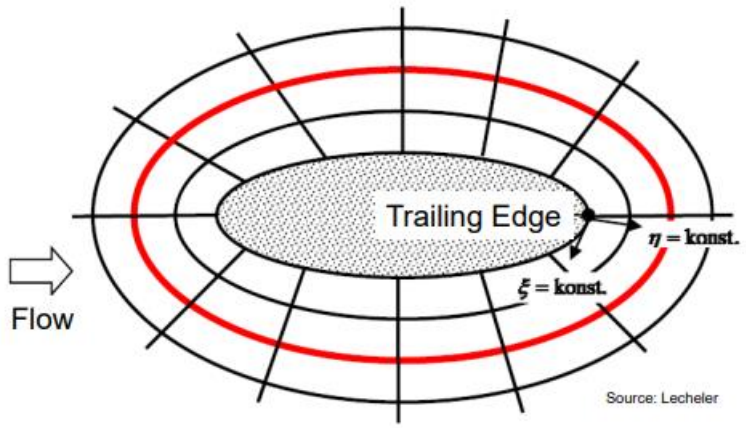

Fig. 19 O grid mesh in the body layer

On the other hand, a structured meshing method is utilized inside the hexacopter in order to capture the intricate flow dynamics and fluctuations located close to the surfaces of the vehicle. When it comes to complex geometries, such as the body of a hexacopter, structured meshes offer superior control and resolution because of the regular grid-like arrangement of its components. In order to simulate the flow that occurs close to the surfaces of the aircraft, a combination of O-grid and C-grid meshes (see in Fig. 19 and Fig. 20) is utilized within the body of the aircraft, together with extremely fine volume elements.

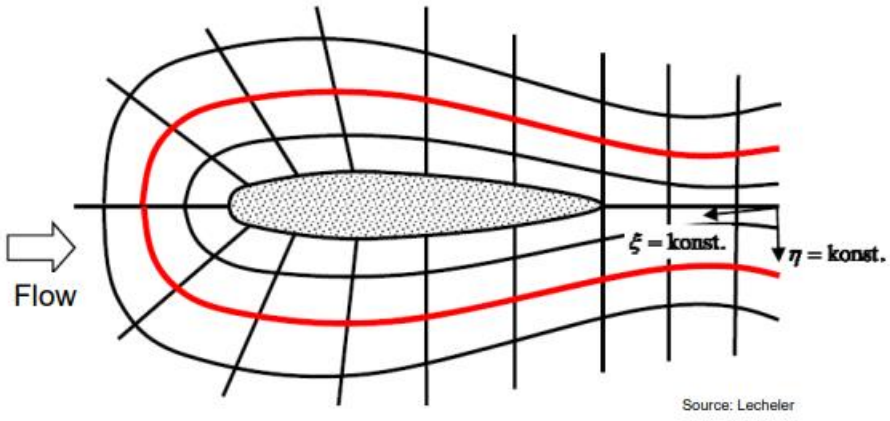

Fig. 20 C grid mesh in the body layer

Structured mesh analysis that is mounted on the body of the helicopter allowed for in-depth flow separation, the formation of boundary layers, and studies of the interplay between aerodynamic flow and surface physics. The computational model captures all flow phenomena the hexacopter faces during flight. This is accomplished by employing a combination of structured and unstructured meshes tailored to the geometric features and flow characteristics of the aircraft and its surroundings.

3.2.3 Setup and modelling using RANS and K- ω SST model

The setup process is intricate and involves several stages, including model and mesh setup, defining boundary conditions, selecting materials, configuring cell zone conditions, and implementing appropriate turbulence models. To accurately capture the aerodynamic behavior of the drone using RANS equations, specifically employing the k-ω Shear Stress Transport (SST) and k-ε models for turbulence simulation.

Section 3.2.3 explains how ANSYS Fluent is configured and how the modelling technique to simulate the urban aerodynamics of a hexacopter drone is applied. The RANS equations, particularly the k-ω SST and k-ε models, are used to configure the material parameters, cell zone conditions, boundary conditions, and to choose a suitable turbulence model. In order to acquire required aerodynamic data (see chapter 4.3), the setup step also involves defining the calculation reports.

The material properties are defined in the initial step of the simulation setup. Air is selected as the working fluid for this investigation. The density and viscosity of air are defined according to the typical conditions described above. These characteristics are essential for a realistic simulation of the hexacopter's surrounding fluid dynamics. This aerodynamic analysis requires precise flow calculations solve by equation (28), which are simplified by treating air because the effect of flow regime is minimal as an incompressible fluid .

The cell zone conditions need to be configured next. The computational domain distinguishes between a solid zone including the hexacopter's body and propellers and a fluid zone containing the surrounding environment. Applying this differentiation, it is certain that regions are given different physical models (see Fig. 21). In this approach, the solid zones are considered impermeable and have an effect on the flow field; in contrast, the fluid zones are responsible for solving the flow equations in (22).

The hexacopter's operation in an airflow is modeled in ANSYS Fluent by configuring the cell zone conditions to match reality. Air qualities are assigned to the fluid zone, while the solid zones, which represent the hexacopter's construction, are defined with the right material properties which are mostly carbon-fibre. The hexacopter's interactions with the surrounding airflow are accurately simulated within this configuration according to the guidelines of the project “EILT”.

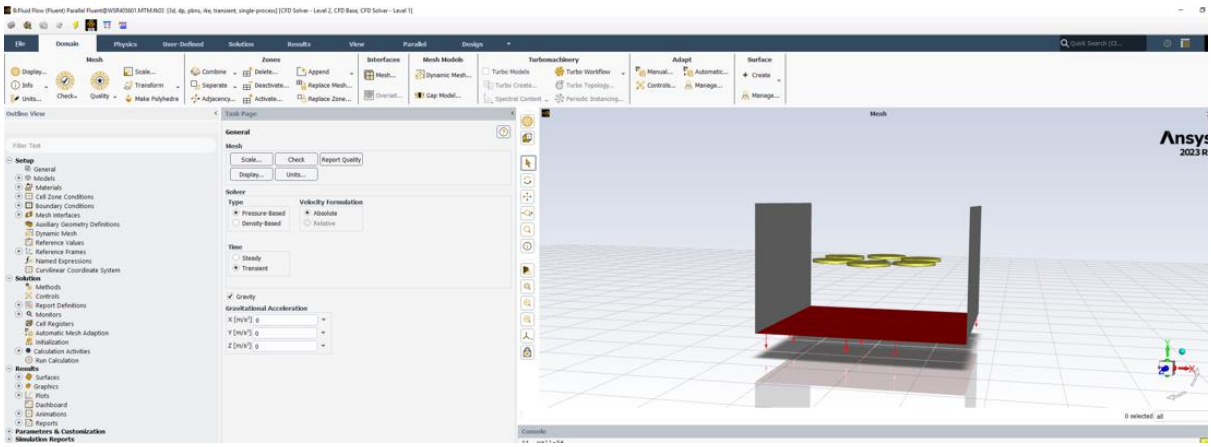

Fig. 21 Initial situation of the simulation conditions

Prior to configuring the flow environment in the simulation, it is essential to define the boundary conditions. The drone's real-time wind data are used to specify the inlet and outlet boundary conditions. Reflecting the wind's speed and direction, the inlet boundary condition specifies the incoming air's velocity or pressure. Ensuring a continuous and smooth flow, the outlet boundary condition permits the air to leave the computational area.

Both the rotor blades and the hexacopter's body are subject to flying wall circumstances. Precise control over the aerodynamic interactions between the blades and the airflow is achieved by treating each propeller blade as an independent wall. A hexacopter's blades and body are experiencing zero relative air velocity due to the no-slip constraint enforced by the wall circumstances. To capture the propellers' lift and drag forces precisely, this setup is required.

A k-ω SST model and a k-ε model are two variants of the RANS technique that are employed in the turbulence model. While both models have a solid foundation in CFD for modelling turbulent flows, their features and uses are somewhat different. Capturing boundary layer events and transitioning to free-stream turbulence are areas where the k- ω SST model shines. The benefits of the k- ω model in the wall regions and the free-stream robustness are combined within. According to Menter (1994), the k- ω SST model can simulate the aerodynamic forces (see modeling in Fig. 22) acting on a hexacopter in a city setting with turbulent and highly variable flow conditions because of its hybrid approach, which enables it to manage complicated flow separations and reattachments. Due to its computing efficiency and simplicity, the k-ε model is commonly employed in contrast. Several engineering applications involving turbulent flows can benefit from its decent accuracy. Nevertheless, in situations when there are substantial negative pressure gradients and flow separations, it

might not accurately represent the near-wall effects compared to the k- ω SST model (Jones & Launder, 1972). Regarding this thesis considering named pro and cons, the k- ω SST model is applied.

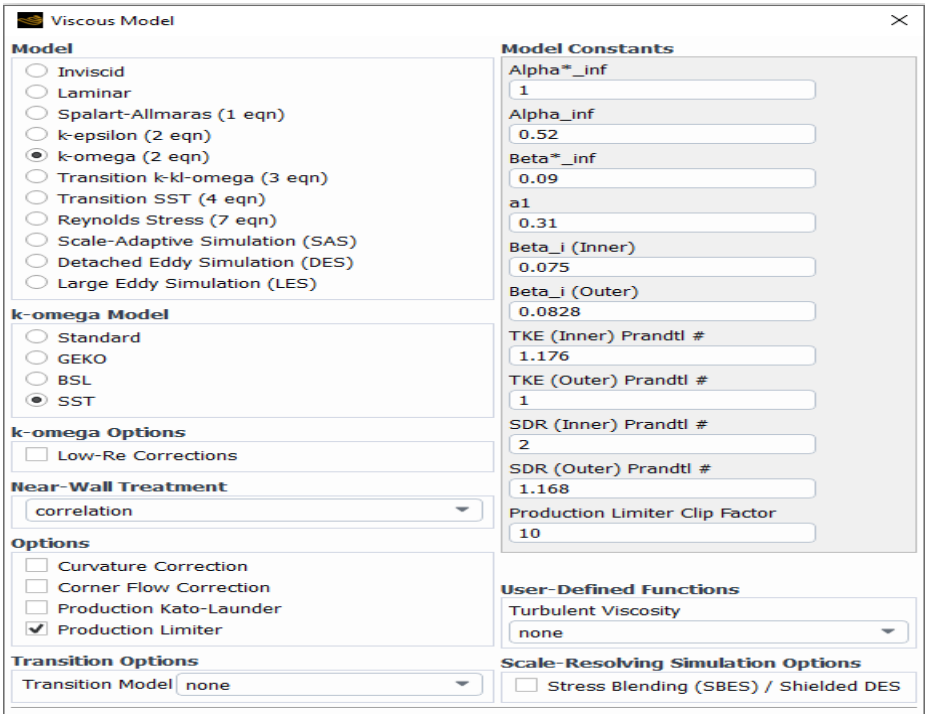

Fig. 22 Turbulence model selection

The shear-stress transport (SST) k-$\boldsymbol{\omega}$ model is employed since it is capable of blending the robust efficiently and formulating the k-$\boldsymbol{\omega}$ model accurately in the near-wall region with the freestream independence in the far-field (Maani et al., 2018, Menter, 1994). It has an identical structure to the standard k-$\boldsymbol{\omega}$ model and is described by the equations (20) and (21)

$$\frac{\partial}{\partial \mathrm{t}}(\rho k)+\frac{\partial}{\partial \mathrm{xi}}(\rho k u_i)=\frac{\partial}{\partial \mathrm{xj}}(\Gamma_k \frac{\partial \mathrm{k}}{\partial \mathrm{xj}})+G_k-Y_k+S_k \tag{20}$$

$$\frac{\partial}{\partial \mathrm{t}}(\rho \omega)+\frac{\partial}{\partial \mathrm{xi}}(\rho \omega u_i)=\frac{\partial}{\partial \mathrm{xj}}(\Gamma_\omega \frac{\partial \omega}{\partial \mathrm{xj}})+G_\omega-Y_\omega+S_\omega+\mathrm{D}_\omega \tag{21}$$

Where, D_ω is the cross-diffusion term. The turbulent viscosity μ_t is calculated as follows:

$$\mu_t=\frac{\rho \mathrm{k}}{\omega}\frac{1}{\max[\frac{1}{\alpha*},\frac{\mathrm{SF2}}{\alpha 1 \omega}]} \tag{22}$$

Where,

$$\sigma_k = \frac{1}{\frac{F1}{\sigma k,1}+\frac{(1-F1)}{\sigma k,2}}$$

and

$$\sigma_\omega = \frac{1}{\frac{F1}{\sigma \omega,1}+\frac{(1-F1)}{\sigma \omega,2}}$$

Here, the blending functions in this case are $F1$ and $F2$. A turbulent kinetic energy creation is represented by the symbol G_k and the minimum value of G_k is equal to:

$$G_k = \min(G_k, 10\rho\beta * k\omega) \tag{23}$$

and, G_ω is the formation of ω and is given by:

$$G_\omega = \frac{\alpha}{vt} G_k \tag{24}$$

The standard k- and standard k-$\boldsymbol{\varepsilon}$ models are both necessary for the k- ω SST model to work. In order for these two models to work together effectively, the traditional k-$\boldsymbol{\varepsilon}$ model is changed into equations that depend on k. This change indicates the presence of a cross-diffusion factor $D\omega$, which is expressed as such:

$$D_\omega = 2(1 - F1)\rho\sigma_{\omega,2} \frac{1}{\omega} \frac{\partial k}{\partial xj} \frac{\partial \omega}{\partial xj} \tag{25}$$

The model constants required for simulations are depicted in Table 1.

Table 1: Model constants

$\sigma_{k,1}$ = 1.176	$\sigma_{\omega,1}$ = 2.0
$\sigma_{k,2}$ = 1.0	$\sigma_{\omega,2}$ = 1.168
a_1 = 0.31, $\beta_{i,1}$ = 0.075	$\beta_{i,2}$ = 0.0828
k = 0.41	

Here, the k-$\boldsymbol{\omega}$ SST model has similar values as for the standard k-$\boldsymbol{\omega}$ model. The simulation needs to dictate the selection and configuration of the turbulence models in ANSYS Fluent as guided by the mathematical procedure. At the boundary, depending on empirical data or

assumptions from similar research, are defined as the starting turbulence values, like turbulent kinetic energy (k) and specific dissipation rate (ω) for the k-ω SST model, or the dissipation rate (ε) for the k-ε model.

Configuring the data reporting and starting settings follows the setup of the physical and boundary conditions. In this case, the lift force, drag force, lift coefficients, and drag coefficients data gathered within the simulations by using the reported settings and to comprehend the hexacopter's operation in different wind scenarios.

By choosing the turbulence model, the simulation is computationally run to solve the RANS equations. Solving the flow equations at each time step is an integral part of the iterative process until convergence is reached. To guarantee a steady and precise solution, convergence criteria are established using the equations' residuals.

4 Results

Using the k- ω SST turbulence model, chapter 4 provides a complete study of the hexacopter's flow field. This analysis begins with tagging the wind parameters for computational modeling. The geometrical identity of the hexacopter is identified for the simulation. Followed by visualizing the streamlines and velocity contours to emphasize the flow behavior around the propellers and body and identified areas of high and low velocity. To show the aerodynamic loading on the hexacopter's surfaces, pressure contours and coefficients are presented. In order to prove that the model can forecast complicated aerodynamic events, it provides incorporate turbulence quantification, which involves displaying turbulence kinetic energy and Reynolds stresses to depict the hexacopter's turbulence distribution and intensity.

4.1 Wind related parameter identification

The primary work demands to get real wind data in urban scenario which is taken by the “Optokopter” at the international airport in Oberpfaffenhofen/Germany. A csv file containing half an hour's worth of flight data is exported and is visualized.

The amount of time that has passed since the measurement or recording session began is usually shown (see in Fig. 23) in the elapsed time column. The unit of measurement is

seconds. It is visible that the longitude coordinates, which give you the exact east-west location of the measuring site. In degrees, points east of the Prime Meridian are represented by positive values, and points west of the Meridian are represented by negative values.

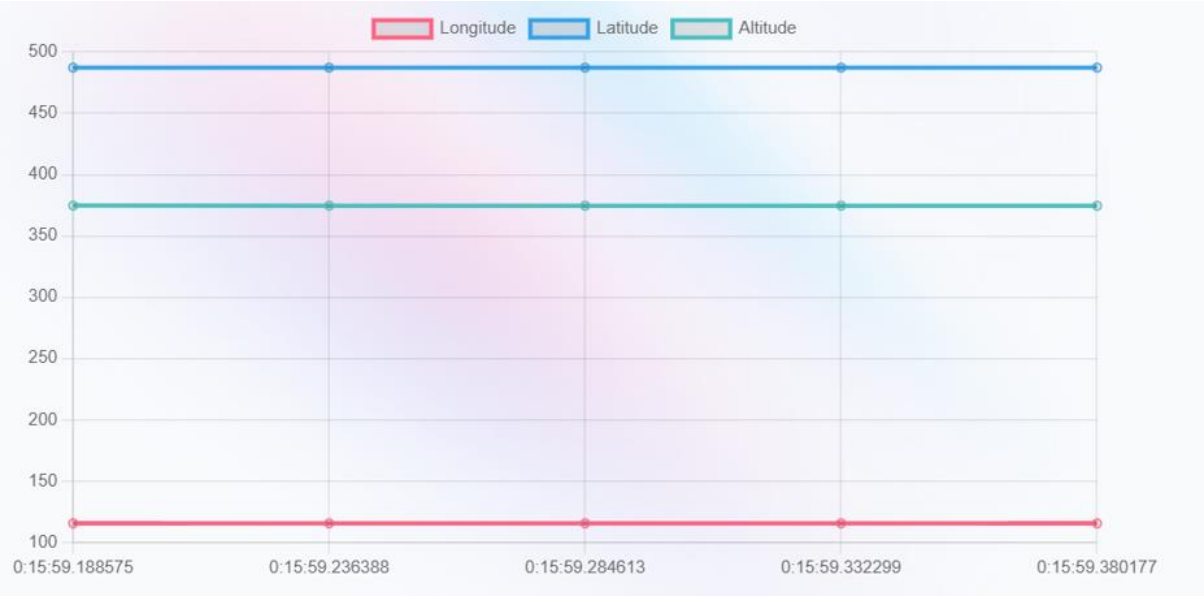

Fig. 23 Optokopter position dataplot

The three-dimensional components of the wind vector are represented by the values in the direction of u, v, and w rows (see in Fig. 24). The wind speed component in an east-west direction is represented as u, or the zonal wind component. When the value is positive, the wind is blowing eastward; when the value is negative, the wind is blowing westward. The meridional wind component is a representation of the wind speed component moving north-south. When the value is positive, the wind is blowing northward; when the value is negative, the wind is blowing southward. The vertical wind component or w is a representation of the wind speed component. Air is said to be moving upward when the value is positive and downhill when it is negative.

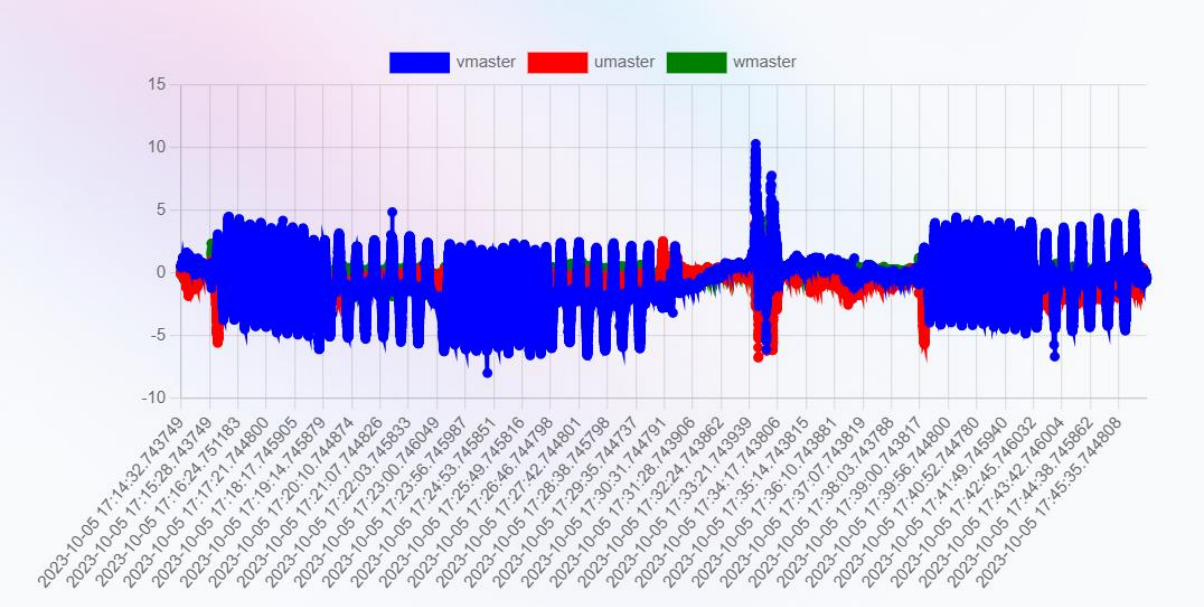

Fig. 24 Optocoter velocity dataplot in u, v and w direction

The author uses these elements together to find the general wind direction and speed. The three-dimensional Pythagorean theorem can be used to determine the wind speed, V (*Flight Control Math 4 Using the Pythagorean Theorem*):

$$V = \sqrt{u^2 + v^2 + w^2} \tag{26}$$

Without considering the vertical component, the horizontal wind speed, V_h, can be computed as follows:

$$V = \sqrt{u^2 + v^2} \tag{27}$$

The arctangent function can be used to find the wind direction (azimuth angle, θ) in the horizontal plane:

$$\theta = \arctan\left(\frac{v}{u}\right) \tag{28}$$

This equation need to be adapted depending on which quadrant contains the values of u and v.

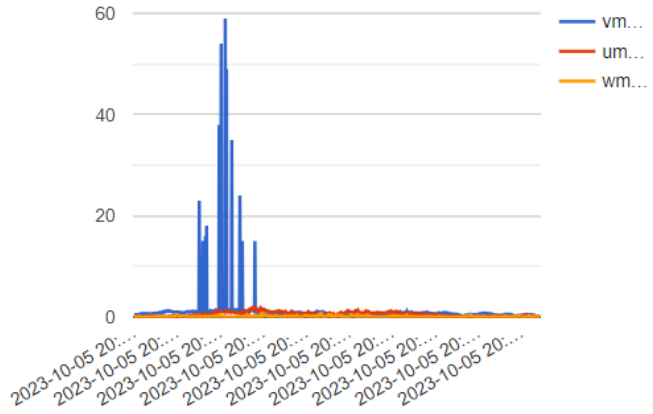

GPSTime	vmaster	umaster	wmaste
2023-10-05 20:14:32	0.54	0.14	0.04
2023-10-05 20:14:32	0.52	0.16	0.03
2023-10-05 20:14:32	0.52	0.12	0.04
2023-10-05 20:14:32	0.53	0.09	0.1
2023-10-05 20:14:32	0.52	0.08	0.09
2023-10-05 20:14:32	0.52	0.07	0.07
2023-10-05 20:14:32	0.52	0.06	0.09
2023-10-05 20:14:32	0.48	0.07	0.09
2023-10-05 20:14:32	0.48	0.03	0.08
2023-10-05 20:14:32	0.48	0.01	0.11
2023-10-05 20:14:32	0.4	0.01	0.17

Fig. 25 Optokopter velocity coordinated to relevant GPSTime

The time based on GPS data is shown (see Fig. 25) in the column “GPSTime”. It shows the precise time the measurement is taken according to the GPS system's clock (UTC time) and is formatted in the standard format (e.g., HH:MM: SS). Measurements can be synchronized with other datasets or events. Measured wind velocities describing the direction by their notation u, v and w shown in this figures table named as vmaster, umaster and wmaster. The value north of the Equator is represented by a positive degree, whereas the value south of the Equator is represented by a negative degree. Altitude shows the height in relation to some ground identified by the on-board barometer of the drone which can vary by up to ±5m due to pressure shift caused by strong winds but is typically located around mean sea level (MSL).

4.2 Body Parameters of the drone

When compared to quadcopters, the hexacopter's six rotors give it superior stability, lifting capability, and redundancy. The efficiency, agility, and performance of a hexacopter are greatly affected by its body parameters. The geometric dimensions, weight, engine specifications, propeller details, frame material, battery capacity, blade profile, and height are all part of these criteria.

- *Frame:* In order to distribute the load and the propulsion evenly among all six rotors, a hexacopter's frame usually takes the shape of a symmetrical hexagon. A crucial factor influencing stability and payload capacity is the frame size. Both the stability and the ability to carry bigger payloads are improved by a larger frame, while the agility and suitability for operations in confined spaces are enhanced by a smaller frame.

- *Carrying Capacity and Weight:* Everything from the frame to the motors, propellers, battery, ESCs, and any other hardware like sensors or cameras adds up to the hexacopter's total weight. Flight time, maneuverability, and power consumption are all directly affected by weight, making it a vital component. Because its thrust is shared across six engines, the hexacopter are capable of carrying large payloads. Depending on the design and motor specifications, this typical payload capacity is around 4 kg. With the right motor and battery choices, a hexacopter can fly steadily even when carrying a 1 kg payload, bringing the total weight to 3 kg.
- *Details about the Engine:* The hexacopter's motors are its beating soul; they provide the push that allows the aircraft to take flight and turn. Because they are efficient, dependable, and need little maintenance, brushless DC motors see extensive use. Thrust, voltage, and current ratings are some of the criteria that should be considered while selecting a motor. Hexacopter uses motors rated of 1200 KV, which is the number of revolutions per minute per volt. Large hexacopters with hefty payloads are better suited to lower KV motors (about 700-900 KV) due to their ability to drive larger propellers more effectively and generate more torque.
- *Features of the Propeller:* A motor's thrust is directly proportional to the RPM of its propellers. Important factors influencing the hexacopter's performance are the propellers' size and pitch. It is designed for heavy lift have larger propellers, with 15 inches in diameter, which allow them to produce more thrust at lower RPM, leading to greater efficiency. The pitch is the distance a propeller would go in one revolution if slippage were not an issue; it is measured in inches. The thrust is greater at a higher pitch, but the power required is higher as well. For balancing thrust and efficiency is a 12x4.5-inch propeller, which has a diameter of 12 inches and a pitch of 4.5 inches.
- *Blade shape:* Another important component that affects aerodynamic performance is the propeller blade profile. How much lift is generated and how efficiently thrust is converted is dependent on the form and cross-chapter of the blades. There are two main types of profiles: symmetrical and asymmetrical. Asymmetrical blades are designed for this particular flight regimes, providing more efficiency and lift but less versatility than symmetrical blades, which are more versatile and consistently perform better in all kinds of flying conditions.
- *Construction of the Frame:* The longevity, mass, and performance of the hexacopter are all impacted by the material that makes up its frame. Aluminum, carbon fiber, and

plastic composites are common materials. The combination of carbon fiber's light weight, strength, and stiffness makes it an ideal material for hexacopters designed for extreme performance. On the other hand, it's pricier than other materials.

- *Battery Storage and Control:* An important factor in flight duration and power availability is the battery. Because of their high discharge rates and energy density, Lithium Polymer (LiPo) battery has been utilized in this hexacopter. Power output and voltage are both defined by the battery's capacity, which is expressed in milliampere-hours (mAh), and the number of cells (S). This hexacopter can benefit greatly from the extended flying time and power offered by a 6S (22.2V) battery with a 5000mAh capacity. Achieving a balance between capacity and weight is crucial for maximum performance, as the choice of battery also impacts the weight.
- *Motor Control Units (MCUs):* ESCs manage the speed and ensure that the motors are operating in synchronus by regulating the power that is provided to each motor. The hexacopter's responsiveness and efficiency are affected by the ESCs' parameters, which include current rating and firmware features. Motor specs and total power needs dictate the typical current rating of an ESC, which can range from 30A to 40A. Modern electronic speed controllers.

4.3 Lift and Drag forces

Checking the transient response to the lift and drag parameters of the hexacopter is done by analyzing the system's reaction to step changes. This entails checking the system's responsiveness to unexpected shifts in inputs or commands for control. The steps (see Fig. 26) to keep an eye out for are as follows:

- The system's reaction to a quick change in input, like a change in the intended drag or lift force, is called the step response. The parameters can be used to describe the step response.
- The time it takes for the response to increase from a low value to a high value, typically between 10% and 90% of the final value, is called the rise time. How long it takes for the result to settle within a predetermined margin (usually 2% or 5% of the ultimate value) is called the settling time.
- Responding to the lift parameter is critical for flying steadily and at a constant altitude. When studying the transient response for lift, one must examine the

accuracy and speed with which the lift force reaches the target level following a step change (see Fig. 26)

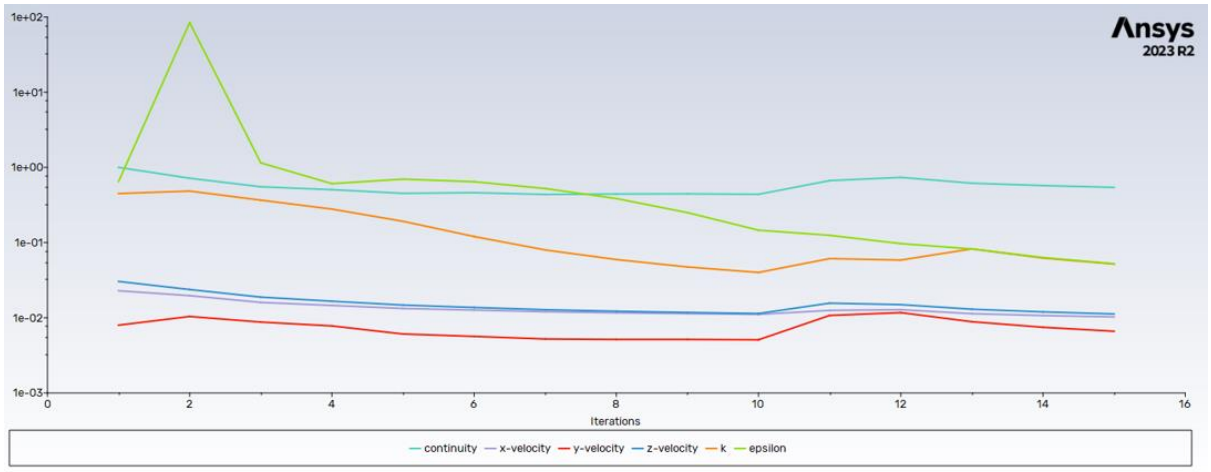

Fig. 26 Result iterations according to the time step

The force (see Fig. 27), exerted on each blade, the coefficients, and the momentum are all drag characteristics that influence the Hexacopter's controllability and efficiency. Securing low energy loss and precise navigation is ensured by a good transient response in these parameters.

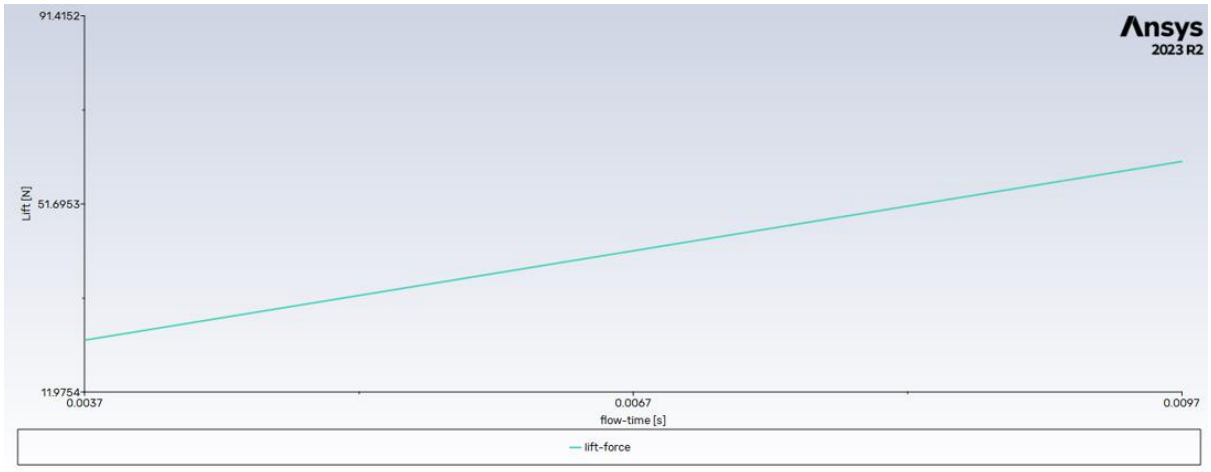

Fig. 27 Rise of simulated lift force depending on the flowtime [s]

According to the Ansys computation, lift above 50N has been seen during 1.5 minutes of flow time. This observation implies that the hexacopter performed significantly aerodynamically during the simulated flight. A vital aerodynamic metric called lift force describes the vertical force produced by an aircraft's rotors or wings, which is required to defy gravity and maintain flight. The hexacopter produces a significant upward force when it achieves lift of more than 50N, most likely as a result of effective airflow over its wings or

propellers. This outcome shows that the hexacopter can generate enough lift to maintain its weight, possibly carry a few more payloads, and endure unfavorable weather.

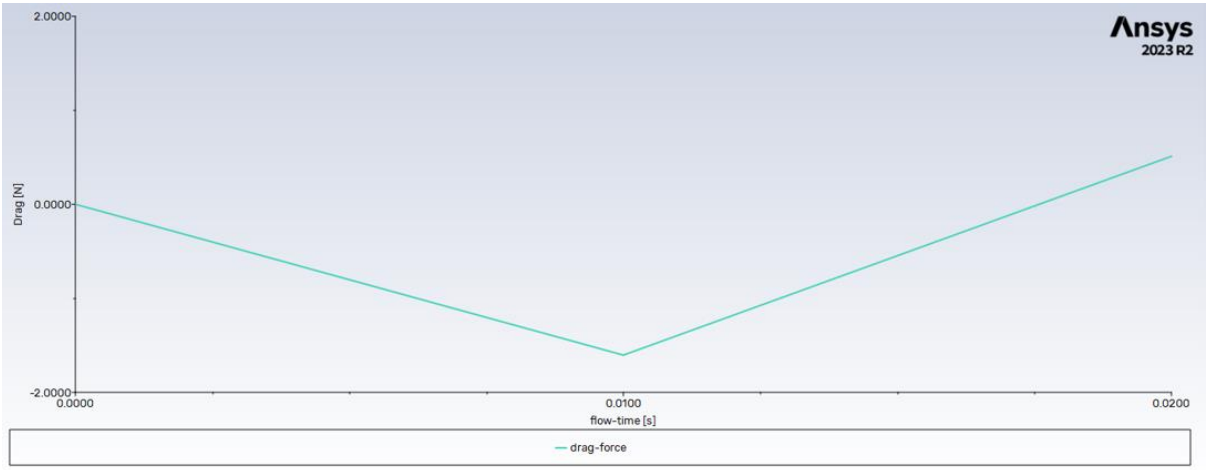

Fig. 28 Course of drag force depending on the flow-time [s]

It appears that there are dynamic changes in the aerodynamic forces acting on the hexacopter during the simulated flight, as evidenced by the observation of drag steadily increasing over time, albeit to a very tiny drag value (see in Fig. 28) of 1N within the same period of lift generation. A streamlined airflow or less resistance at takeoff may be indicated by the drag force, which is the aircraft's resistance due to air friction and other variables, initially decreasing. But the rise in drag that follows indicates a change in aerodynamic conditions, which could be brought in by adjustments to airspeed, angle of attack, or surrounding airflow patterns.

The calculated coefficients from Ansys are (see in Fig. 30,31) :

- Lift coefficient, $C_l > 96$
- Drag coefficient, $C_d < -2.0$

4.3.1 Components of total aerodynamic forces

This subsection presents the hexacopter's aerodynamic performance. A part of this is the pressure-velocity contour plots (see in Fig. 29), which show the distribution of the two variables around the drone's structure graphically. In addition, the evaluation of the moments max 10000 Nm operating on the entire drone (A_x, A_y, A_z) sheds light on the flight dynamics of stability and control. The instant concerning is the x-axis (20 Nm). It is possible to account for probable asymmetries or yawing tendencies by obtaining a negligible moment of 1 Nm for the moment about the y-axis (yaw), which is a balanced aerodynamic configuration in

stable flight conditions. Similarly, a tiny moment of 2 Nm is obtained for the moment around the z-axis (roll), which indicates a slight tendency for the hexacopter to roll in the absence of notable disruptions or asymmetries. These hypotheses provide a simplified understanding of the aerodynamic stability and balance of the hexacopter; actual values may differ depending on design details, flight dynamics, and outside circumstances. All these findings show how the hexacopter performs and behaves aerodynamically in urban areas.

The Ansys computed Moments are about (see in Fig 32);

- X-axis – 20 Nm
- Y-axis – 1 Nm
- Z-axis - 2 Nm

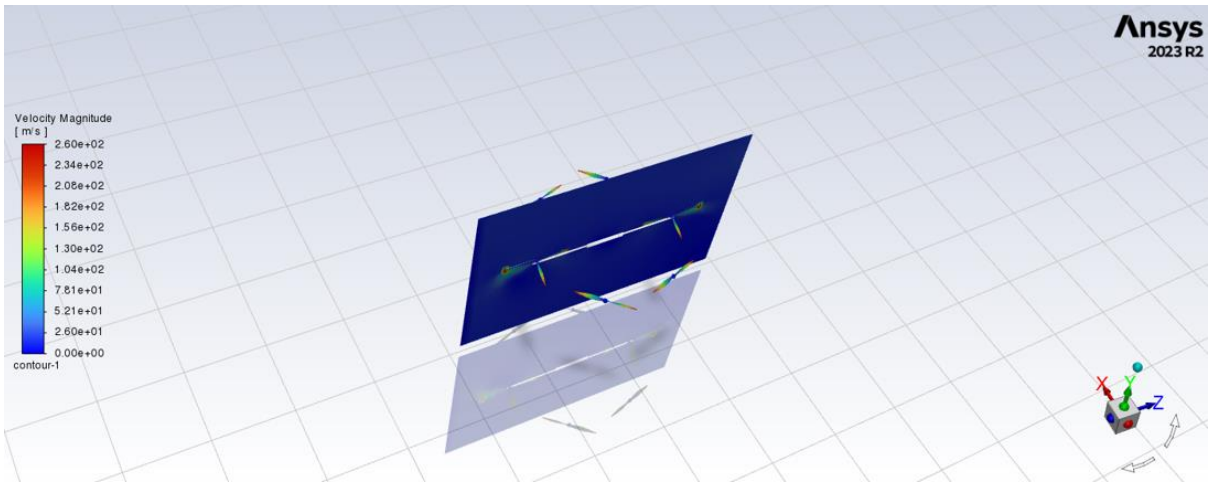

Fig. 29 Velocity contour

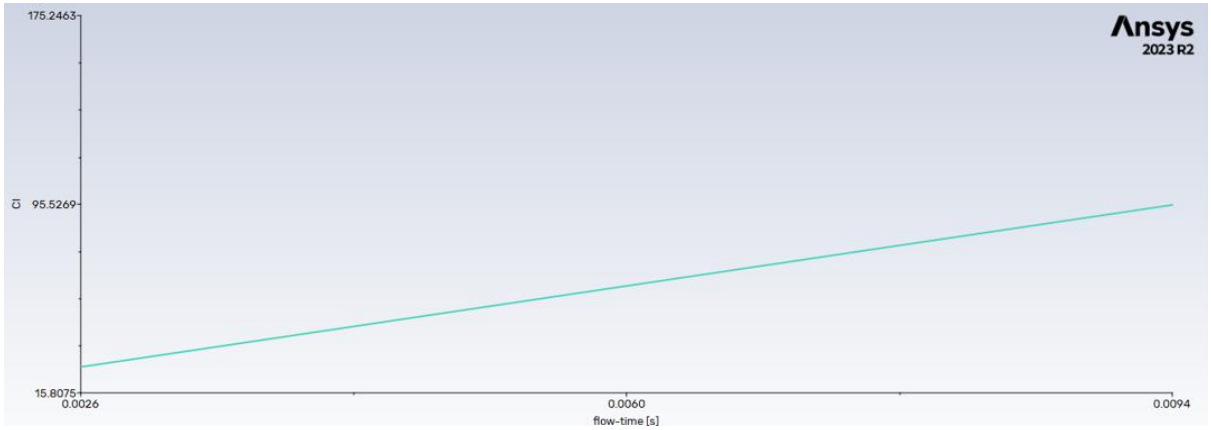

Fig. 30 Lift coefficient(c_l) data

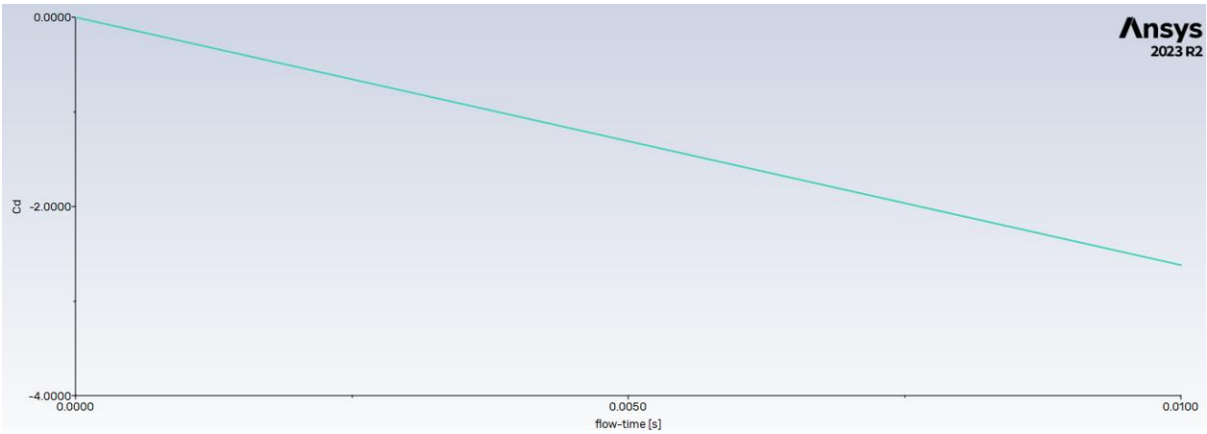

Fig. 31 Drag coefficient(c_d) data

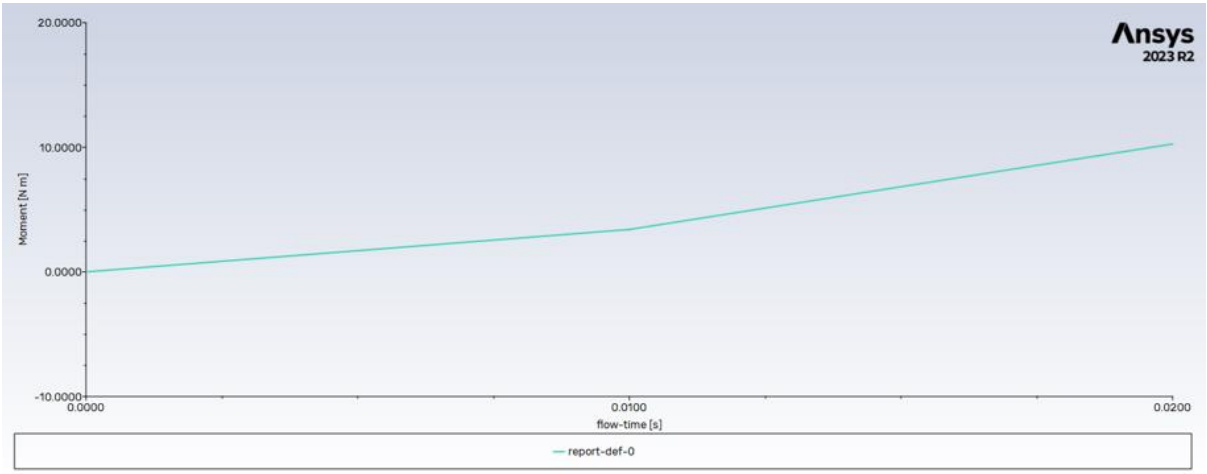

Fig. 32 Moment action data

5 Discussion

This thesis has done a comprehensive analysis, utilizing experimental and computational approaches, of the aerodynamic forces acting on a hexacopter drone in urban areas. Drone flights in a simulated airport setting yield physical data that provides a baseline, capturing the UAV's interaction with wind speed and turbulence impacts. In order to validate the ANSYS Fluent CFD simulations, these empirical data points are crucial.

The computational study is thorough, beginning with fixing and refining the CAD geometry of the hexacopter and ending with a complex meshing technique to accurately describe the flow domain. Precise prediction of aerodynamic behaviors in intricate urban environments is made possible by incorporating the k-ω SST turbulence model into the RANS framework, which allows for a detailed comprehension of the interplay between near-wall and freestream flows. The resulting equations and incorporation of blending functions demonstrate that the k- ω SST model, with its combination of precision and resilience, is especially good at describing the turbulence features surrounding the drone. According to the research, the k ω - SST model outperforms the k-ε model in these simulations because it iterates with better precision.

Detailed pressure-velocity contours are displayed in the data, which demonstrate the complex flow patterns surrounding the hexacopter. The moments operating on the entire drone, combined with the computed lift forces of 49N, 48N, 47N, 45N, and 47N for the blades, give quantitative insights into the UAV's aerodynamic performance and stability under different conditions. The results show that the k- ω SST model is good at recreating aerodynamic phenomena in the actual world and also confirm the experimental findings. Even though the drag is still not as great as the lift, this pattern shows how dynamic the aerodynamic forces are that the hexacopter encountered during the flight simulation.

It is also covered that how the results can affect future plans for UAV operations in crowded city skies, both in terms of design and strategy. In order to improve the stability and efficiency of UAVs, sophisticated turbulence modeling is necessary, as shown by the aerodynamic forces and moments that have been identified.

6 Conclusion

To conclude, a combination of experimental data and CFD models, this thesis delves deeply into the aerodynamic performance of a hexacopter drone in city settings. By combining real-world drone flights with ANSYS Fluent models, it is possible to research more about the aerodynamic forces and flow dynamics that affected the UAV in the urban region. The research proves that the k- ω SST model is good at forecasting aerodynamic behaviors, especially when it comes to capturing turbulence effects surrounding the drone, by carefully fixing the geometry, meshing, and modeling turbulence. Gaining a comprehensive understanding of the UAV's aerodynamic performance and stability is made possible by the obtained pressure-velocity contours, moments, lift and drag coefficients. The CFD method is shown to be reliable and has predictive powers when compared to experimental data. Practical implications for the design and operation of drones in urban areas are offered by the findings of this thesis, which also contribute to furthering the understanding of UAV aerodynamics. This research establishes a strong groundwork for future studies and applications in urban UAV operations by clarifying the intricate relationship between flow dynamics and UAV aerodynamics. The importance of interdisciplinary approaches in solving real-world problems and improving UAV capabilities is emphasized throughout this thesis. Future research and practical applications in urban UAV operations can be informed by this thesis's rigorous methodological framework and empirical validation.

References

1. Vasile, P. (2016, September 8). *CFD Analysis of UAV Flying Wing*. INCAS Buletin. https://doi.org/10.13111/2066-8201.2016.8.3.6
2. Yilmaz, E., & Hu, J. (2018, April 28). *CFD Study of Quadcopter Aerodynamics at Static Thrust Conditions*. ResearchGate. https://www.researchgate.net/publication/328007354_CFD_Study_of_Quadcopter_Aerodynamics_at_Static_Thrust_Conditions
3. Dodson, M. G., & Miklosovic, D. (2005, January). *A Historical and Applied Aerodynamic Study of the Wright Brothers' Wind Tunnel Test Program and Application to Successful Manned Flight*. Retrieved May 24, 2024, from https://www.researchgate.net/publication/267496036_An_Historical_and_Applied_Aerodynamic_Study_of_the_Wright_Brothers'_Wind_Tunnel_Test_Program_and_Application_to_Successful_Manned_Flight
4. Bistafa, S. R. (2017, November). *On the development of the Navier-Stokes equation by Navier*. Researchgate. Retrieved May 24, 2024, from https://www.researchgate.net/publication/321396111_On_the_development_of_the_Navier-Stokes_equation_by_Navier
5. Herath, P., Jin, H., Bai, X., & Thatcher, M. (2021, September). *Effectiveness of urban surface characteristics as mitigation strategies for the excessive summer heat in cities*. Researchgate. Retrieved May 24, 2024, from https://www.researchgate.net/publication/352357126_Effectiveness_of_urban_surface_characteristics_as_mitigation_strategies_for_the_excessive_summer_heat_in_cities
6. Noor, N. M., Abdullah, A., & Hashim, M. (2018, July 31). *Remote sensing UAV/drones and its applications for urban areas: a review*. IOP Conference Series. Earth and Environmental Science. https://doi.org/10.1088/1755-1315/169/1/012003
7. Ohashi, M. (2004, January 1). *A STUDY ON ANALYSIS OF AIRFLOW AROUND AN INDIVIDUAL TREE*. Nihon Kenchiku Gakkai Kankyokei Ronbunshu. https://doi.org/10.3130/aije.69.91_2
8. Bhattacharyya, S., Abraham, J., Cheng, L., & Gorman, J. M. (2022, October 26). *Introductory Chapter: A Brief History of and Introduction to Computational Fluid Dynamics*. IntechOpen eBooks. https://doi.org/10.5772/intechopen.97235
9. Sheng, W. (2020, March 1). *A revisit of Navier–Stokes equation*. European Journal of Mechanics. B, Fluids. https://doi.org/10.1016/j.euromechflu.2019.12.005
10. Sadrehaghighi, I. (2023, April). *Aerodynamic Basics*. Researchgate. Retrieved May 24, 2024, from https://www.researchgate.net/publication/339499388_Aerodynamic_Basics
11. Katz, J., & Plotkin, A. (2004, March). *Low-Speed Aerodynamics, Second Edition*. Researchgate. Retrieved May 24, 2024, from https://www.researchgate.net/publication/245356726_Low-Speed_Aerodynamics_Second_Edition
12. https://www.researchgate.net/publication/314584837_Dynamics_Control_and_Planning_for_Cooperative_Manipulation_of_Payloads_Suspended_by_Cables_from_Multiple_Quadrotor_Robots
13. Mane, S. (2023, June 24). *Theoretical Overview on Aerodynamic Forces & Flexibility*. ResearchGate. https://www.researchgate.net/publication/371811670_Theoretical_Overview_on_Aerodynamic_Forces_Flexibility
14. *Lift and Drag*. (2017, November 3). https://doi.org/10.1002/9781118534786.ch7

15. Yongcai, L. (2016, January 1). *An Efficient Paving Method of Pure Quad Mesh Generation*. ResearchGate. Yongcai, I. (2016, January). *An Efficient Paving Method of Pure Quad Mesh Generation*. Researchgate. Retrieved May 24, 2024, from https://www.researchgate.net/publication/316991532_An_Efficient_Paving_Method_of_Pure_Quad_Mesh_Generation.
16. *Introduction to Ansys ICEM CFD*. (n.d.). Ansys. Retrieved April 25, 2024, from https://www.ansys.com/training-center/course-catalog/fluids/introduction-to-ansys-icem-cfd
17. Boutchko, R., Sitek, A., & Gullberg, G. T. (2013, April 15). *Practical implementation of tetrahedral mesh reconstruction in emission tomography*. Physics in Medicine & Biology/Physics in Medicine and Biology. https://doi.org/10.1088/0031-9155/58/9/3001
18. Sun, L., Yeh, G. T., & Zhao, G. (2017, May 1). *Applications of quadrilateral and quadrilateral-prism mesh generation in overland and subsurface simulations*. Journal of Hydrology. https://doi.org/10.1016/j.jhydrol.2017.02.048
19. *Solving dynamic equations in dye transport*. (2014, January 1). Elsevier eBooks. https://doi.org/10.1533/9780857097583.100
20. *Defense Technical Information Center*. (n.d.). https://apps.dtic.mil/sti/citations/ADA127801
21. *The Finite Volume Method in Computational Fluid Dynamics*. (n.d.). SpringerLink. https://link.springer.com/book/10.1007/978-3-319-16874-6
22. *An Introduction to Computational Fluid Dynamics*. (n.d.). Google Books. https://books.google.de/books/about/An_Introduction_to_Computational_Fluid_D.html?id=RvBZ-UMpGzIC&redir_esc=y
23. Liu, C., & Hu, C. (2018, April 1). *An adaptive multi-moment FVM approach for incompressible flows*. Journal of Computational Physics. https://doi.org/10.1016/j.jcp.2018.01.006
24. Li, Z., & Wang, S. (1999, June 1). *The finite volume method and application in combinations*. Journal of Computational and Applied Mathematics. https://doi.org/10.1016/s0377-0427(99)00051-5
25. Gottlieb, S., & Ketcheson, D. I. (2016, January 1). *Time Discretization Techniques*. Handbook of Numerical Analysis. https://doi.org/10.1016/bs.hna.2016.08.001
26. Ascher, U. M., Ruuth, S. J., & Spiteri, R. J. (1997, November 1). *Implicit-explicit Runge-Kutta methods for time-dependent partial differential equations*. Applied Numerical Mathematics. https://doi.org/10.1016/s0168-9274(97)00056-1
27. Serra, N., & Semião, V. (2021, October 1). *ESIMPLE, a new pressure–velocity coupling algorithm for built-environment CFD simulations*. Building and Environment. https://doi.org/10.1016/j.buildenv.2021.108170
28. *Flight Control Math 4 Using the Pythagorean Theorem*. (n.d.). *Flight Control Math 4 Using the Pythagorean Theorem*. (n.d.-b). NASA. https://www.nasa.gov/stem-content/flight-control-math-4-using-the-pythagorean-theorem/
29. Telefónica. (2022, September 9). *What drones are and their valuable service to society*. Telefónica. https://www.telefonica.com/en/communication-room/blog/what-drones-are-and-their-valuable-service-to-society/#:~:text=While%20their%20military%20purpose%20remains,infrastructure%20inspections%2C%20science%2C%20the%20fight
30. Ecko. (2023, June 13). *The Advantages of UAVs: Revolutionizing Industries and Shaping the Future*. https://www.linkedin.com/pulse/advantages-uavs-revolutionizing-industries-shaping-future-

ecko360#:~:text=Precise%20Mapping%20and%20Surveying%3A%20UAVs,consuming%20and%20prone%20to%20errors.

Appendices

Preparing mesh for display,

```
Done.

Preparing mesh for display...
Note: zone-surface: cannot create surface from sliding interface zone.
Creating empty surface.
Note: zone-surface: cannot create surface from sliding interface zone.
Creating empty surface.
Note: zone-surface: cannot create surface from sliding interface zone.
Creating empty surface.
Note: zone-surface: cannot create surface from sliding interface zone.
Creating empty surface.
Note: zone-surface: cannot create surface from sliding interface zone.
Creating empty surface.
Note: zone-surface: cannot create surface from sliding interface zone.
Creating empty surface.
Note: zone-surface: cannot create surface from sliding interface zone.
Creating empty surface.
Note: zone-surface: cannot create surface from sliding interface zone.
Creating empty surface.
Note: zone-surface: cannot create surface from sliding interface zone.
Creating empty surface.
Note: zone-surface: cannot create surface from sliding interface zone.
Creating empty surface.
Note: zone-surface: cannot create surface from sliding interface zone.
Creating empty surface.
Note: zone-surface: cannot create surface from sliding interface zone.
Creating empty surface.
Done.
```

Selection of wall zone,

```
**  wall-54
**  wall-51
**  wall-48
**  wall-45
**  wall-42
**  wall-39
**  wall-38
**  outlet_2
** Found Following new zones in the current mesh:
**  outlet2
**  inlet2
**  inlet1
**  wall-40
**  wall-43
**  wall-46
**  wall-49
**  wall-52
**  wall-55
**  wall-56
**
** Please ensure that your current Setup is valid.
************************************************************************
************************************************************************

Model Information is incompatible with incoming mesh.
Found some missing and new zones in the mesh. To make mesh compatible with settings, please visit "Match Zone Names" panel
(File->Recorded Mesh Operations->Edit Incoming Zones... -> Match Zone Names...).
"Model Information is incompatible with incoming mesh.
Found some missing and new zones in the mesh. To make mesh compatible with settings, please visit "Match Zone Names" panel
(File->Recorded Mesh Operations->Edit Incoming Zones... -> Match Zone Names...)."
```

Calculation running,

Console

```
    10  4.3856e-01  1.1084e-02  5.0934e-03  1.1384e-02  4.0052e-02  1.4610e-01  0:04:25   10
    11  6.6680e-01  1.2534e-02  1.0729e-02  1.5629e-02  6.1203e-02  1.2480e-01  0:04:10    9

 turbulent viscosity limited to viscosity ratio of 1.000000e+05 in 2 cells
    12  7.3680e-01  1.2789e-02  1.1693e-02  1.4943e-02  5.8534e-02  9.6898e-02  0:03:40    8

 Reversed flow on 2 faces (0.2% area) of pressure-outlet 101.

 turbulent viscosity limited to viscosity ratio of 1.000000e+05 in 6 cells
    13  6.1588e-01  1.1330e-02  8.8515e-03  1.2991e-02  8.2396e-02  8.2158e-02  0:03:09    7

 Reversed flow on 1 face (0.1% area) of pressure-outlet 101.

 turbulent viscosity limited to viscosity ratio of 1.000000e+05 in 22 cells
    14  5.7293e-01  1.0694e-02  7.4658e-03  1.1969e-02  6.2211e-02  6.3206e-02  0:02:41    6

 turbulent viscosity limited to viscosity ratio of 1.000000e+05 in 30 cells
    15  5.4205e-01  1.0253e-02  6.6132e-03  1.1229e-02  5.1771e-02  5.2261e-02  0:02:13    5

 turbulent viscosity limited to viscosity ratio of 1.000000e+05 in 32 cells
    16  5.2200e-01  9.9395e-03  6.1094e-03  1.0683e-02  4.3488e-02  4.6660e-02  0:01:45    4
```

Console

```
    15  5.4205e-01  1.0253e-02  6.6132e-03  1.1229e-02  5.1771e-02  5.2261e-02  0:02:13    5

 turbulent viscosity limited to viscosity ratio of 1.000000e+05 in 32 cells
    16  5.2200e-01  9.9395e-03  6.1094e-03  1.0683e-02  4.3488e-02  4.6660e-02  0:01:45    4

 turbulent viscosity limited to viscosity ratio of 1.000000e+05 in 28 cells
    17  5.0816e-01  9.6983e-03  5.8114e-03  1.0304e-02  3.7957e-02  4.2749e-02  0:01:19    3

 turbulent viscosity limited to viscosity ratio of 1.000000e+05 in 25 cells
    18  4.9786e-01  9.5342e-03  5.6279e-03  1.0025e-02  3.4844e-02  4.1532e-02  0:00:52    2

 turbulent viscosity limited to viscosity ratio of 1.000000e+05 in 17 cells
    19  4.8875e-01  9.3911e-03  5.4973e-03  9.8008e-03  3.0031e-02  3.7869e-02  0:00:26    1

 turbulent viscosity limited to viscosity ratio of 1.000000e+05 in 9 cells
    20  4.8208e-01  9.2593e-03  5.4120e-03  9.6075e-03  2.8285e-02  3.6286e-02  0:00:00    0
(update-animation-object "animation-1")
Creating animation sequence file: D:/Joy/Drone - Kopie/DRONE_files/dp0/FFF-1/Fluent/.//animation-1.cxa
()

Writing to WSR405601:"D:\Joy\Drone - Kopie\DRONE_files\dp0\FFF-1\Fluent\FFF-3-00002.cas.h5" in NODE0 mode and compression level 1 ...
Grouping cells for Laplace smoothing ...
     4376969 cells,     7 zones ...
     9090341 faces,    48 zones ...
      804996 nodes,     1 zone  ...
  Done.
Done.

Writing to WSR405601:"D:\Joy\Drone - Kopie\DRONE_files\dp0\FFF-1\Fluent\FFF-3-00002.dat.h5" in NODE0 mode and compression level 1 ...
  Writing results.
```

Console

```
    13  6.1588e-01  1.1330e-02  8.8515e-03  1.2991e-02  8.2396e-02  8.2158e-02  0:03:09    7

 Reversed flow on 1 face (0.1% area) of pressure-outlet 101.

 turbulent viscosity limited to viscosity ratio of 1.000000e+05 in 22 cells
    14  5.7293e-01  1.0694e-02  7.4658e-03  1.1969e-02  6.2211e-02  6.3206e-02  0:02:41    6

 turbulent viscosity limited to viscosity ratio of 1.000000e+05 in 30 cells
    15  5.4205e-01  1.0253e-02  6.6132e-03  1.1229e-02  5.1771e-02  5.2261e-02  0:02:13    5

 turbulent viscosity limited to viscosity ratio of 1.000000e+05 in 32 cells
    16  5.2200e-01  9.9395e-03  6.1094e-03  1.0683e-02  4.3488e-02  4.6660e-02  0:01:45    4

 turbulent viscosity limited to viscosity ratio of 1.000000e+05 in 28 cells
    17  5.0816e-01  9.6983e-03  5.8114e-03  1.0304e-02  3.7957e-02  4.2749e-02  0:01:19    3

 turbulent viscosity limited to viscosity ratio of 1.000000e+05 in 25 cells
    18  4.9786e-01  9.5342e-03  5.6279e-03  1.0025e-02  3.4844e-02  4.1532e-02  0:00:52    2

 turbulent viscosity limited to viscosity ratio of 1.000000e+05 in 17 cells
    19  4.8875e-01  9.3911e-03  5.4973e-03  9.8008e-03  3.0031e-02  3.7869e-02  0:00:26    1

 turbulent viscosity limited to viscosity ratio of 1.000000e+05 in 9 cells
    20  4.8208e-01  9.2593e-03  5.4120e-03  9.6075e-03  2.8285e-02  3.6286e-02  0:00:00    0
(update-animation-object "animation-1")
Creating animation sequence file: D:/Joy/Drone - Kopie/DRONE_files/dp0/FFF-1/Fluent/.//animation-1.cxa
()

Writing to WSR405601:"D:\Joy\Drone - Kopie\DRONE_files\dp0\FFF-1\Fluent\FFF-3-00002.cas.h5" in NODE0 mode and compression level 1 ...
Grouping cells for Laplace smoothing ...
```

Console

```
   10  4.3856e-01  1.1084e-02  5.0934e-03  1.1384e-02  4.0052e-02  1.4610e-01  0:04:25   10
   11  6.6680e-01  1.2534e-02  1.0729e-02  1.5629e-02  6.1203e-02  1.2480e-01  0:04:10    9

turbulent viscosity limited to viscosity ratio of 1.000000e+05 in 2 cells
   12  7.3680e-01  1.2789e-02  1.1693e-02  1.4943e-02  5.8534e-02  9.6898e-02  0:03:40    8

Reversed flow on 2 faces (0.2% area) of pressure-outlet 101.

turbulent viscosity limited to viscosity ratio of 1.000000e+05 in 6 cells
   13  6.1588e-01  1.1330e-02  8.8515e-03  1.2991e-02  8.2396e-02  8.2158e-02  0:03:09    7

Reversed flow on 1 face (0.1% area) of pressure-outlet 101.

turbulent viscosity limited to viscosity ratio of 1.000000e+05 in 22 cells
   14  5.7293e-01  1.0694e-02  7.4658e-03  1.1969e-02  6.2211e-02  6.3206e-02  0:02:41    6

turbulent viscosity limited to viscosity ratio of 1.000000e+05 in 30 cells
   15  5.4205e-01  1.0253e-02  6.6132e-03  1.1229e-02  5.1771e-02  5.2261e-02  0:02:13    5

turbulent viscosity limited to viscosity ratio of 1.000000e+05 in 32 cells
   16  5.2200e-01  9.9395e-03  6.1094e-03  1.0683e-02  4.3488e-02  4.6660e-02  0:01:45    4

turbulent viscosity limited to viscosity ratio of 1.000000e+05 in 28 cells
   17  5.0816e-01  9.6983e-03  5.8114e-03  1.0304e-02  3.7957e-02  4.2749e-02  0:01:19    3

turbulent viscosity limited to viscosity ratio of 1.000000e+05 in 25 cells
   18  4.9786e-01  9.5342e-03  5.6279e-03  1.0025e-02  3.4844e-02  4.1532e-02  0:00:52    2

turbulent viscosity limited to viscosity ratio of 1.000000e+05 in 17 cells
   19  4.8875e-01  9.3911e-03  5.4973e-03  9.8008e-03  3.0031e-02  3.7869e-02  0:00:26    1
```

Console

```
done.

 iter  continuity  x-velocity  y-velocity  z-velocity           k     epsilon     time/iter
   10  4.3856e-01  1.1084e-02  5.0934e-03  1.1384e-02  4.0052e-02  1.4610e-01  0:04:25   10
   11  6.6680e-01  1.2534e-02  1.0729e-02  1.5629e-02  6.1203e-02  1.2480e-01  0:04:10    9

turbulent viscosity limited to viscosity ratio of 1.000000e+05 in 2 cells
   12  7.3680e-01  1.2789e-02  1.1693e-02  1.4943e-02  5.8534e-02  9.6898e-02  0:03:40    8

Reversed flow on 2 faces (0.2% area) of pressure-outlet 101.

turbulent viscosity limited to viscosity ratio of 1.000000e+05 in 6 cells
   13  6.1588e-01  1.1330e-02  8.8515e-03  1.2991e-02  8.2396e-02  8.2158e-02  0:03:09    7

Reversed flow on 1 face (0.1% area) of pressure-outlet 101.

turbulent viscosity limited to viscosity ratio of 1.000000e+05 in 22 cells
   14  5.7293e-01  1.0694e-02  7.4658e-03  1.1969e-02  6.2211e-02  6.3206e-02  0:02:41    6

turbulent viscosity limited to viscosity ratio of 1.000000e+05 in 30 cells
   15  5.4205e-01  1.0253e-02  6.6132e-03  1.1229e-02  5.1771e-02  5.2261e-02  0:02:13    5

turbulent viscosity limited to viscosity ratio of 1.000000e+05 in 32 cells
   16  5.2200e-01  9.9395e-03  6.1094e-03  1.0683e-02  4.3488e-02  4.6660e-02  0:01:45    4

turbulent viscosity limited to viscosity ratio of 1.000000e+05 in 28 cells
   17  5.0816e-01  9.6983e-03  5.8114e-03  1.0304e-02  3.7957e-02  4.2749e-02  0:01:19    3

turbulent viscosity limited to viscosity ratio of 1.000000e+05 in 25 cells
   18  4.9786e-01  9.5342e-03  5.6279e-03  1.0025e-02  3.4844e-02  4.1532e-02  0:00:52    2
```

Step response and calculations

Console

```
  step  flow-time report-def-0  lift-force   lift-data   flow-time  drag-force draft-coeffi
     1  1.0000e-02  3.4026e+00  6.2257e+01  1.0164e+02  1.0000e-02 -1.6045e+00 -2.6196e+00
Flow time = 0.01s, time step = 1
99 more time steps

Updating solution at time level N...
 done.

  iter  continuity  x-velocity  y-velocity  z-velocity           k     epsilon     time/iter
    10  4.3856e-01  1.1084e-02  5.0934e-03  1.1384e-02  4.0052e-02  1.4610e-01  0:04:25   10
    11  6.6680e-01  1.2534e-02  1.0729e-02  1.5629e-02  6.1203e-02  1.2480e-01  0:04:10    9

 turbulent viscosity limited to viscosity ratio of 1.000000e+05 in 2 cells
    12  7.3680e-01  1.2789e-02  1.1693e-02  1.4943e-02  5.8534e-02  9.6898e-02  0:03:40    8

 Reversed flow on 2 faces (0.2% area) of pressure-outlet 101.

 turbulent viscosity limited to viscosity ratio of 1.000000e+05 in 6 cells
    13  6.1588e-01  1.1330e-02  8.8515e-03  1.2991e-02  8.2396e-02  8.2158e-02  0:03:09    7

 Reversed flow on 1 face (0.1% area) of pressure-outlet 101.

 turbulent viscosity limited to viscosity ratio of 1.000000e+05 in 22 cells
    14  5.7293e-01  1.0694e-02  7.4658e-03  1.1969e-02  6.2211e-02  6.3206e-02  0:02:41    6

 turbulent viscosity limited to viscosity ratio of 1.000000e+05 in 30 cells
    15  5.4205e-01  1.0253e-02  6.6132e-03  1.1229e-02  5.1771e-02  5.2261e-02  0:02:13    5

 turbulent viscosity limited to viscosity ratio of 1.000000e+05 in 32 cells
    16  5.2200e-01  9.9395e-03  6.1094e-03  1.0683e-02  4.3488e-02  4.6660e-02  0:01:45    4
```

Uploading solutions,

Console

```
  Writing results.
Done.
Open existing project file for writing: D:\Joy\Drone - Kopie\DRONE_files\dp0\FFF-1\Fluent\FFF.flprj
  step  flow-time report-def-0  lift-force   lift-data   flow-time  drag-force draft-coeffi
     1  1.0000e-02  3.4026e+00  6.2257e+01  1.0164e+02  1.0000e-02 -1.6045e+00 -2.6196e+00
Flow time = 0.01s, time step = 1
99 more time steps

Updating solution at time level N...
 done.

  iter  continuity  x-velocity  y-velocity  z-velocity           k     epsilon     time/iter
    10  4.3856e-01  1.1084e-02  5.0934e-03  1.1384e-02  4.0052e-02  1.4610e-01  0:04:25   10
    11  6.6680e-01  1.2534e-02  1.0729e-02  1.5629e-02  6.1203e-02  1.2480e-01  0:04:10    9

 turbulent viscosity limited to viscosity ratio of 1.000000e+05 in 2 cells
    12  7.3680e-01  1.2789e-02  1.1693e-02  1.4943e-02  5.8534e-02  9.6898e-02  0:03:40    8

 Reversed flow on 2 faces (0.2% area) of pressure-outlet 101.

 turbulent viscosity limited to viscosity ratio of 1.000000e+05 in 6 cells
    13  6.1588e-01  1.1330e-02  8.8515e-03  1.2991e-02  8.2396e-02  8.2158e-02  0:03:09    7

 Reversed flow on 1 face (0.1% area) of pressure-outlet 101.

 turbulent viscosity limited to viscosity ratio of 1.000000e+05 in 22 cells
    14  5.7293e-01  1.0694e-02  7.4658e-03  1.1969e-02  6.2211e-02  6.3206e-02  0:02:41    6

 turbulent viscosity limited to viscosity ratio of 1.000000e+05 in 30 cells
    15  5.4205e-01  1.0253e-02  6.6132e-03  1.1229e-02  5.1771e-02  5.2261e-02  0:02:13    5
```

Grouping cells for Laplace smoothing,

```
Console
Grouping cells for Laplace smoothing ...
     4376969 cells,     7 zones ...
     9089393 faces,    48 zones ...
      804996 nodes,     1 zone  ...
  Done.
Done.

Writing to WSR405601:"D:\Joy\Drone - Kopie\DRONE_files\dp0\FFF-1\Fluent\FFF-3-00001.dat.h5" in NODE0 mode and compression level 1 ...
  Writing results.
Done.
Open existing project file for writing: D:\Joy\Drone - Kopie\DRONE_files\dp0\FFF-1\Fluent\FFF.flprj
  step  flow-time report-def-0  lift-force   lift-data   flow-time  drag-force draft-coeffi
     1  1.0000e-02  3.4026e+00  6.2257e+01  1.0164e+02  1.0000e-02 -1.6045e+00 -2.6196e+00
Flow time = 0.01s, time step = 1
99 more time steps

Updating solution at time level N...
 done.

  iter  continuity  x-velocity  y-velocity  z-velocity           k     epsilon     time/iter
    10  4.3856e-01  1.1084e-02  5.0934e-03  1.1384e-02  4.0052e-02  1.4610e-01  0:04:25   10
    11  6.6680e-01  1.2534e-02  1.0729e-02  1.5629e-02  6.1203e-02  1.2480e-01  0:04:10    9

 turbulent viscosity limited to viscosity ratio of 1.000000e+05 in 2 cells
    12  7.3680e-01  1.2789e-02  1.1693e-02  1.4943e-02  5.8534e-02  9.6898e-02  0:03:40    8

 Reversed flow on 2 faces (0.2% area) of pressure-outlet 101.

 turbulent viscosity limited to viscosity ratio of 1.000000e+05 in 6 cells
    13  6.1588e-01  1.1330e-02  8.8515e-03  1.2991e-02  8.2396e-02  8.2158e-02  0:03:09    7
```

All Force result,

```
Console
Zone                            Pressure                                  Viscous                                   Total
Viscous                                  Total
bladel                          (-0.31231411 49.461881 -0.35274028)       (-0.0036431192 -0.094229249 -0.0011830683)    (-0.31595723 49.367652
80.754091 -0.57590249)                (-0.0059479496 -0.15384367 -0.0019315401)     (-0.51584854 80.600248 -0.57783403)
blade_2                         (0.120767 48.253748 -0.36708862)          (0.002096511 -0.095927998 -0.011175226)       (0.12286351 48.15782 -
78.78163 -0.59932835)                 (0.0034228751 -0.15661714 -0.018245267)       (0.20059348 78.625013 -0.61757362)
blade_3                         (0.56396818 47.646932 -0.10612233)        (0.04267291 -0.11037565 -0.021989509)         (0.60664109 47.536556
77.790909 -0.17326095)                (0.069670057 -0.18020514 -0.035901239)        (0.99043444 77.610704 -0.20916219)
blade_4                         (0.9339149 47.440291 1.0048214)           (-0.016116034 -0.081921626 0.0055389093)      (0.91779887 47.358369
77.453536 1.6405248)                  (-0.026311892 -0.13374959 0.0090431172)       (1.4984471 77.319787 1.6495679)
blade_5                         (-0.41781534 45.872409 1.5112329)         (0.011223896 -0.075414984 -0.021139499)       (-0.40659144 45.796994
74.893728 2.4673191)                  (0.018324727 -0.1231265 -0.034513468)         (-0.66382277 74.770602 2.4328056)
blade_6                         (-0.50136821 47.803114 0.091941091)       (0.021324154 -0.079078907 -0.0068075707)      (-0.48004406 47.724035
78.0459 0.1501079)                    (0.034814945 -0.12910842 -0.011114401)        (-0.7837454 77.916792 0.1389935)
------------------------- ------------------------------------------ ----------------------------------------- ----------------------
-------------------------------------------- ------------------------------------------ ----------------------------------------

Net                             (0.38715242 286.47837 1.7820442)          (0.057558317 -0.53694841 -0.056755964)        (0.44471074 285.94143
467.71979 2.90946)                    (0.093972763 -0.87665047 -0.092662799)        (0.72605835 466.84314 2.8167972)

Forces - Direction Vector (0 1 0)
                                Forces [N]                                Coefficients
Zone                            Pressure        Viscous         Total     Pressure        Viscous         Total
bladel                          49.461881       -0.094229249    49.367652 80.754091       -0.15384367     80.600248
blade_2                         48.253748       -0.095927998    48.15782  78.78163        -0.15661714     78.625013
blade_3                         47.646932       -0.11037565     47.536556 77.790909       -0.18020514     77.610704
blade_4                         47.440291       -0.081921626    47.358369 77.453536       -0.13374959     77.319787
blade_5                         45.872409       -0.075414984    45.796994 74.893728       -0.1231265      74.770602
blade_6                         47.803114       -0.079078907    47.724035 78.0459         -0.12910842     77.916792
------------------------- --------------- --------------- --------------- --------------- --------------- ---------------
Net                             286.47837       -0.53694841     285.94143 467.71979       -0.87665047     466.84314
```

Setup display,

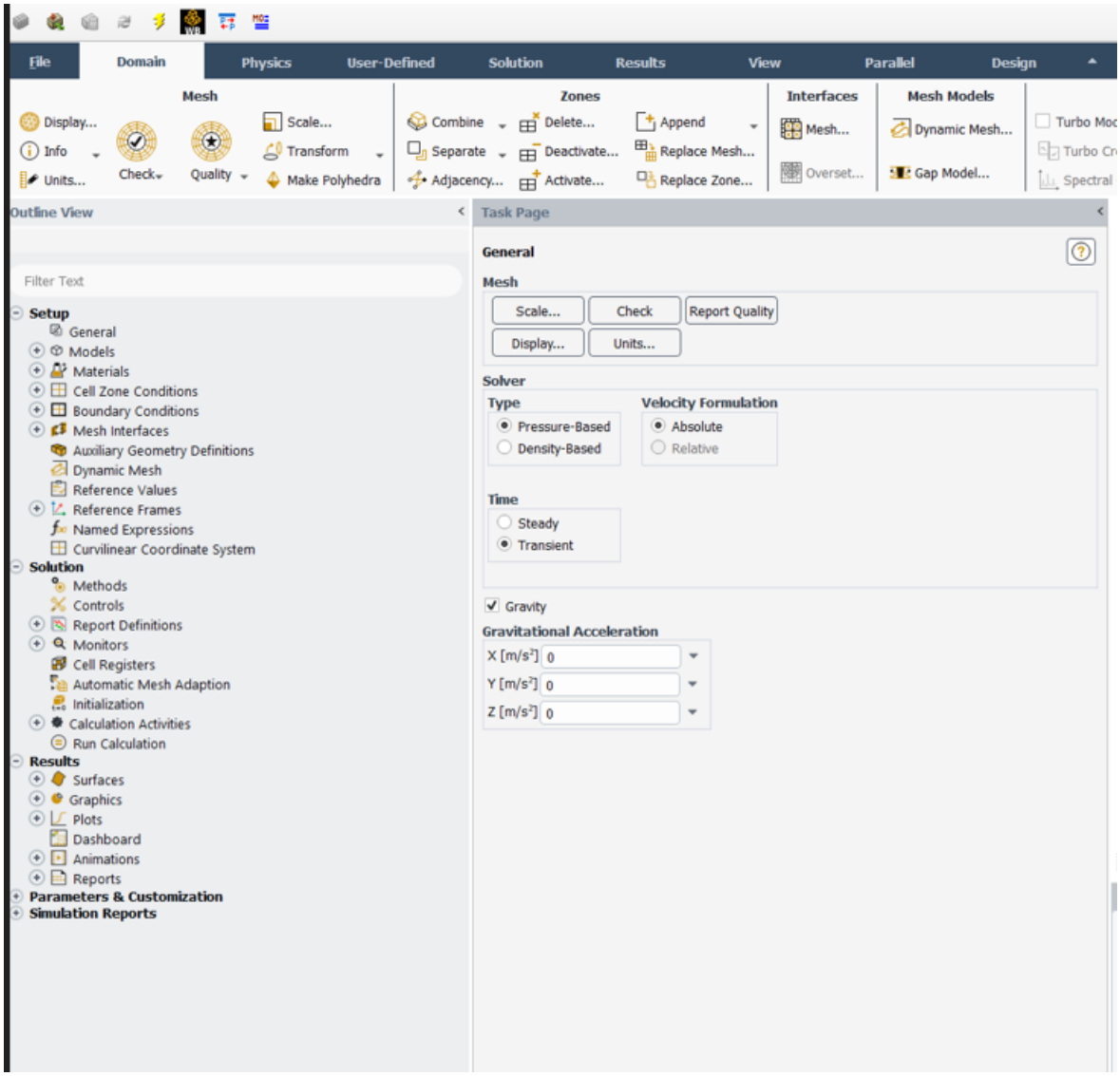

Report printing,